BIOCHEMISTRY

A pan-coronavirus fusion inhibitor targeting the HR1 domain of human coronavirus spike

Shuai Xia[1]*, Lei Yan[2]*, Wei Xu[1]*, Anurodh Shankar Agrawal[3], Abdullah Algaissi[3,4], Chien-Te K. Tseng[3], Qian Wang[1], Lanying Du[5], Wenjie Tan[6], Ian A. Wilson[2,7†], Shibo Jiang[1,5†], Bei Yang[2†], Lu Lu[1†]

Copyright © 2019 The Authors, some rights reserved; exclusive licensee American Association for the Advancement of Science. No claim to original U.S. Government Works. Distributed under a Creative Commons Attribution NonCommercial License 4.0 (CC BY-NC).

Continuously emerging highly pathogenic human coronaviruses (HCoVs) remain a major threat to human health, as illustrated in past SARS-CoV and MERS-CoV outbreaks. The development of a drug with broad-spectrum HCoV inhibitory activity would address this urgent unmet medical need. Although previous studies have suggested that the HR1 of HCoV spike (S) protein is an important target site for inhibition against specific HCoVs, whether this conserved region could serve as a target for the development of broad-spectrum pan-CoV inhibitor remains controversial. Here, we found that peptide OC43-HR2P, derived from the HR2 domain of HCoV-OC43, exhibited broad fusion inhibitory activity against multiple HCoVs. EK1, the optimized form of OC43-HR2P, showed substantially improved pan-CoV fusion inhibitory activity and pharmaceutical properties. Crystal structures indicated that EK1 can form a stable six-helix bundle structure with both short α-HCoV and long β-HCoV HR1s, further supporting the role of HR1 region as a viable pan-CoV target site.

INTRODUCTION

Coronaviruses (CoVs) are enveloped viruses with a positive-sense, single-stranded RNA and are associated with various natural hosts. CoVs are divided into alpha, beta, gamma, and delta groups, and the beta group is further composed of A, B, C, and D subgroups (Fig. 1A) (*1*). Among them, six CoVs can infect humans (HCoVs), including HCoV-229E (229E) and HCoV-NL63 (NL63) in the alpha group, HCoV-OC43 (OC43) and HCoV-HKU1 (HKU1) in beta subgroup A, severe acute respiratory syndrome CoV (SARS-CoV) in beta subgroup B, and Middle East respiratory syndrome CoV (MERS-CoV) in beta subgroup C (*2*).

In this century, SARS-CoV and MERS-CoV have emerged in the human population and caused severe pulmonary disease with alarmingly high case-fatality rates. In 2002, SARS-CoV infections first appeared in China and then quickly spread as a global epidemic in more than 30 countries with 8273 infections and 775 deaths (nearly 10% mortality) (*2*). In 2012, MERS-CoV emerged in Saudi Arabia and spread throughout the Middle East. In 2015, the second pandemic of MERS-CoV occurred in South Korea, causing super-spreading events with third- and fourth-generation cases of infection. The World Health Organization has reported 2229 laboratory-confirmed cases of MERS-CoV infection, including 791 deaths (about 35% case fatality) in 27 countries as of August 2018 (www.who.int/emergencies/mers-cov/en/). Meanwhile, the remaining common HCoVs, such as 229E, OC43, and NL63, usually infect the human upper respiratory tract and cause the common cold, but they also are responsible for severe and even fatal diseases in children, elderly, and immunocompromised patients (*3*–*5*). These scenarios suggest that those common HCoVs might also pose a lethal threat to humans. Note that HCoVs are rapidly evolving. OC43 isolates with novel genomes are being continuously identified (*6*–*8*).

The existence of SARS-like CoV (SL-CoV) and MERS-like CoV (ML-CoV) also pose great threats to public health worldwide. Recent studies identified some types of SL-CoV, such as SL-WIV1-CoV and SL-SHC014-CoV, whose spike (S) proteins highly resemble those of SARS-CoV. These SL-CoVs could use the same SARS-CoV receptor, i.e., angiotensin-converting enzyme-2 (ACE2), to directly enter permissive human cells without need for adaptation (*9*–*11*). In addition, the ML-CoV, *Tylonycteris* bat CoV HKU4, was shown to recognize the MERS-CoV receptor CD26 and infect human cells either after introduction of two single mutations (S746R and N762A) into its S protein or with the help of exogenous protease (*12*, *13*). From a historical perspective, zoonotic CoVs harbor a strong ability to cross species barriers to infect humans rapidly and unpredictably, as illustrated by newly emerging HCoVs (*2*, *14*). Thus, developing a specific drug that only targets a single HCoV would be ineffective against newly emerging HCoVs (*9*–*11*). Since no broad-spectrum anti-HCoV drug is currently available for clinical use, it is incumbent to search for a common or conserved target site based on existing HCoVs.

The S glycoprotein is a type I transmembrane glycoprotein that plays an important role in mediating viral infection and is common to all HCoVs. The S proteins consist of two subunits, S1 and S2 (Fig. 1B). The S1 subunit binds the cellular receptor through its receptor-binding domain (RBD), followed by conformational changes in the S2 subunit, which allows the fusion peptide to insert into the host target cell membrane. The heptad repeat 1 (HR1) region in the S2 subunit forms a homotrimeric assembly, which exposes three highly conserved hydrophobic grooves on the surface that

[1]Shanghai Public Health Clinical Center and School of Basic Medical Sciences, and Key Laboratory of Medical Molecular Virology of MOE/MOH, Fudan University, Shanghai 200032, China. [2]Shanghai Institute for Advanced Immunochemical Studies, ShanghaiTech University, Shanghai 201210, China. [3]Department of Microbiology and Immunology, University of Texas Medical Branch, Galveston, TX 77555, USA. [4]Department of Medical Laboratories Technology, College of Applied Medical Sciences, Jazan University, Jazan, Saudi Arabia. [5]Lindsley F. Kimball Research Institute, New York Blood Center, New York, NY 10065, USA. [6]MOH Key Laboratory of Medical Virology, National Institute for Viral Disease Control and Prevention, Chinese Center for Disease Control and Prevention, Beijing, China. [7]Department of Integrative Structural and Computational Biology and the Skaggs Institute for Chemical Biology, The Scripps Research Institute, 10550 North Torrey Pines Road, BCC206, La Jolla, CA 92037, USA.
*These authors contributed equally to this work.
†Corresponding author. Email: wilson@scripps.edu (I.A.W.); shibojiang@fudan.edu.cn (S.J.); yangbei@shanghaitech.edu.cn (B.Y.); lul@fudan.edu.cn (L.L.)

Downloaded from http://advances.sciencemag.org/ on April 10, 2019

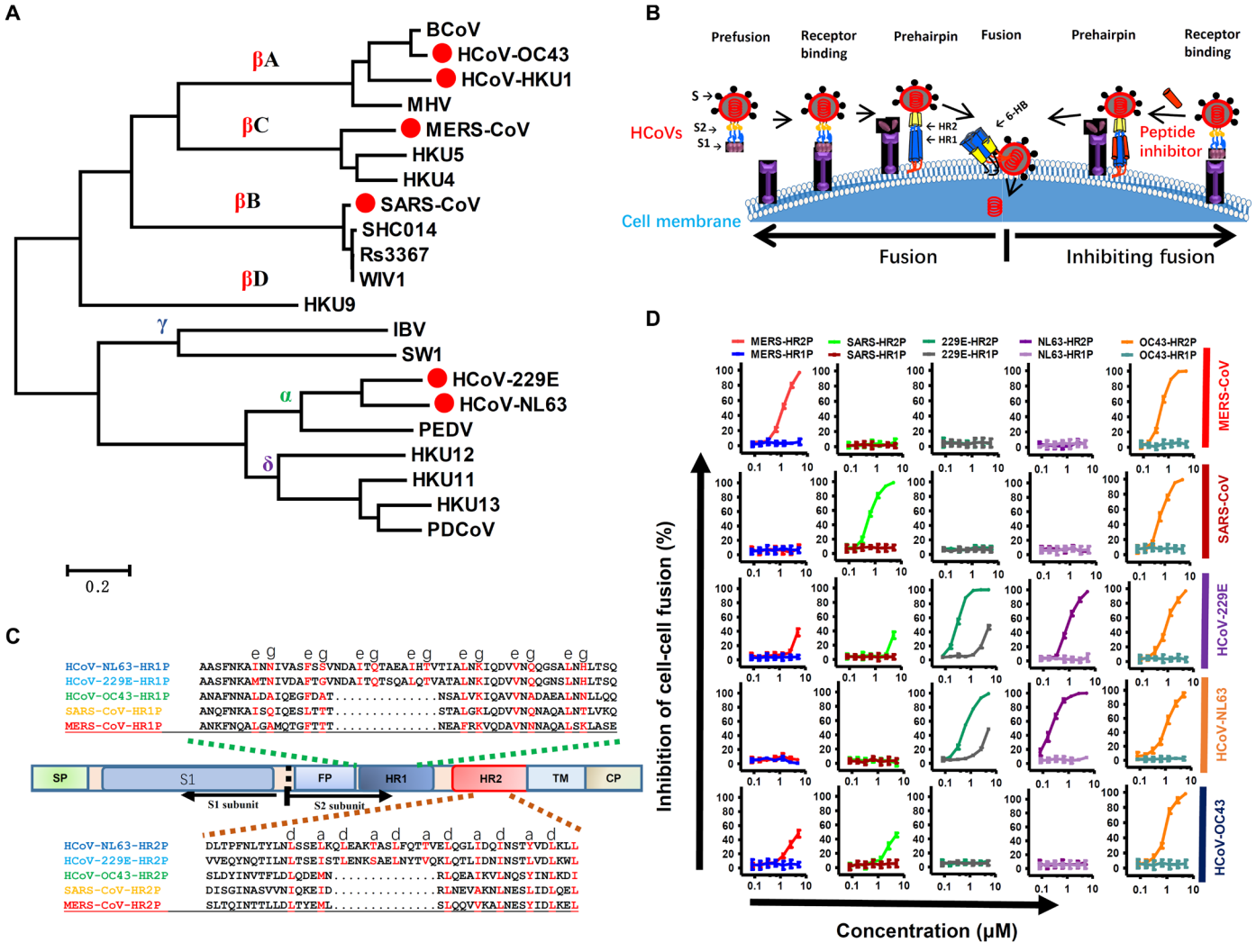

Fig. 1. HR1P and HR2P fusion inhibitory activity. (**A**) Maximum likelihood trees created with the S sequence of representative CoVs from all four genogroups. HCoVs are denoted with filled red circles. (**B**) The antiviral mechanism of HR2P peptides. (**C**) Schematic representation of HCoV S protein. SP, signal peptide; FP, fusion peptide; HR, heptad repeat domain (HR1 and HR2); TM, transmembrane domain; CP, cytoplasmic domain. Corresponding sequences of the designed peptides (HR1Ps and HR2Ps). (**D**) HR2P peptides potently inhibit cell-cell fusion mediated by the S proteins of MERS-CoV, SARS-CoV, 229E, NL63, and OC43. Data are means ± SD of triplicate samples from a representative experiment.

bind heptad repeat 2 (HR2). This six-helix bundle (6-HB) core structure is formed during the fusion process and helps bring the viral and cellular membranes into close proximity for viral fusion and entry (Fig. 1B) (*15*). Thus, the S protein is an important target protein for the development of specific drugs. In particular, the S1 RBD is a very good target site, and both RBD-specific antibodies and RBD-based vaccines have previously exhibited effective antiviral activity or protective effect in blocking binding of virus to host receptors (*16*). However, from an evolutionary perspective, the RBD of CoV is part of a highly mutable region and, thus, is not an ideal target site for broad-spectrum antiviral inhibitor development (*14*). The SARS-CoV RBD-specific antibody fm6 failed to block infection mediated by the S protein of SL-CoV–SHC014 (*9*–*11*, *17*). In contrast, the HR region in the S2 subunit is conserved among various HCoVs and plays a pivotal role in HCoV infections by forming the 6-HB that mediates viral fusion (fig. S1A). Furthermore, the mode of interaction between HR1 and HR2 is conserved among CoVs such that residues located at the "*e*" and "*g*" positions in the HR1 helices interact with residues at the "*a*" and "*d*" positions in the HR2 helices (fig. S1B) (*18*). Previous studies have reported that peptides derived from the HR2 (or C-terminal HR) region of class I viral fusion proteins from some enveloped viruses, including HIV-1 (*19*–*21*), respiratory syncytial virus (RSV) (*22*), Ebola virus (*23*), paramyxoviruses SV5 (*24*), Nipah virus (*25*), and murine hepatitis virus (MHV) (*26*), could competitively bind the viral HR1 (or N-terminal HR) and effectively inhibit viral infection. Therefore, it is reasonable to speculate that HR1 could also be a good target for the development of fusion inhibitors against highly pathogenic HCoVs.

We and others have reported that peptides derived from the HR2 regions of SARS-CoV and MERS-CoV S proteins can competitively inhibit viral 6-HB formation, thereby preventing viral fusion and entry into host cells (*18*, *27*). For example, the peptide CP-1, derived from the SARS-CoV spike protein HR2 region, was able to inhibit SARS-CoV entry in a manner similar to that of MERS-HR2P

Downloaded from http://advances.sciencemag.org/ on April 10, 2019

against MERS-CoV infection (*18*, *27*). However, we note that those peptides lack broad-spectrum antiviral activity against heterologous HCoVs. For example, CP-1 and MERS-HR2P peptides failed to cross-inhibit MERS-CoV and SARS-CoV infection, respectively. Furthermore, the CoV fusion core HR regions can be divided into two groups (*28*, *29*): short HRs, such as MERS-CoV, SARS-CoV, and OC43 HRs; and long HRs, such as 229E and NL63 HRs. The difference between short and long HRs arises from an insertion of 14 amino acids in the long HRs, further increasing the difficulty in designing broad-spectrum peptide fusion inhibitors. To address this challenge, we herein report the successful screening of a peptide OC43-HR2P with broad-spectrum fusion inhibitory activity. Furthermore, a modified OC43-HR2P peptide, EK1, shows promising potency and breadth in inhibiting infection by multiple HCoVs. In vivo studies demonstrate that administration of EK1 via the nasal route exhibits highly protective effects and safety profiles, highlighting its clinical potential. Moreover, structural studies of EK1 in complex with HR1s from different HCoVs explain the conserved basis for the HR1-EK1 interaction, further indicating that HR1 region could serve as a promising target site for the development of broad-spectrum pan-CoV fusion inhibitors.

RESULTS

HR-derived peptides inhibit cell-cell fusion mediated by S proteins of multiple HCoVs

On the basis of the 6-HB fusion core structure, we previously reported on peptides MERS-HR1P and MERS-HR2P that were derived from MERS-CoV HR1 and HR2, respectively (fig. S1C), and these two peptides displayed good interaction with each other (*27*). Here, we located the conserved HR region of multiple HCoVs by sequence comparisons and then synthesized HR1- and HR2-derived peptides, termed HR1P and HR2P (Fig. 1C). Notably, we observed 14–amino acid insertions in both HR1P and HR2P in the HRs of two α-HCoVs, i.e., 229E and NL63.

To systematically assess the inhibitory activities of these peptides against different HCoVs, we developed multiple cell-cell fusion assays that were mediated by the S protein of various HCoVs (fig. S1D). Consistent with previous results, MERS-HR2P had inhibitory activity against cell-cell fusion mediated by MERS-CoV S protein with a concentration for 50% inhibition (IC_{50}) of 1.01 μM, whereas it showed little inhibitory activity in other HCoV S-mediated cell-cell fusion assays even with concentrations up to 5 μM (Fig. 1D and table S1). Similarly, SARS-HR2P specifically inhibited SARS-CoV S-mediated cell-cell fusion with an IC_{50} of 0.52 μM. On the other hand, HR2P peptides derived from the two α-HCoVs, i.e., 229E and NL63, showed potent and broad inhibitory activity against α-HCoV S-mediated cell-cell fusion with IC_{50} values ranging from 0.13 to 0.51 μM or from 0.21 to 0.56 μM, respectively, but no effective inhibitory activity against β-HCoVs (including MERS-CoV, SARS-CoV, and OC43) S-mediated fusion (Fig. 1D and table S1). OC43-HR2P exhibited broad and potent fusion inhibitory activity with IC_{50} values of 0.39, 0.54, and 0.66 μM against MERS-CoV, SARS-CoV, and OC43, respectively (Fig. 1D and table S1). Unexpectedly, OC43-HR2P, a β-HCoV HR2-derived peptide, and thus 14 residues shorter than 229E-HR2P and NL63-HR2P, exhibited effective activity against α-HCoVs with an IC_{50} of 0.84 μM on 229E-S–mediated cell-cell fusion and an IC_{50} of 0.94 μM on NL63-S–mediated cell-cell fusion. Among all HR1Ps, only 229E-HR1P exhibited moderate inhibitory effects on 229E-S– and NL63-S–mediated cell-cell fusion (Fig. 1D). Thus, compared to HR1Ps, all HCoV HR2-derived peptides exhibited excellent self-specific fusion inhibitory activity, whereas OC43-HR2P showed broad-spectrum and potent fusion inhibitory activity against both α-HCoV and β-HCoV S-mediated cell-cell fusion (Fig. 1D and table S1). We also measured the α-helicity of OC43-HR2P and HCoV-HR1Ps by circular dichroism and found that the peptides alone exhibited limited α-helicity ranging from 11.3 to 42.3% (fig. S1E). In contrast, the mixtures of OC43-HR2P and each of these HR1 peptides, respectively, exhibited high α-helicity (70.9 to 86.7%) with melting transition temperature (T_m) values that ranged from 48.5° to 91.5°C (fig. S1E), further implying that OC43-HR2P can bind HR1s of different HCoVs and form stable complexes, thereby blocking S protein–mediated fusion.

EK1, a modified OC43-HR2P peptide, has improved fusion inhibitory activity and increased solubility

It was previously reported that introduction of negatively and positively charged amino acids Glu (E) and Lys (K), at the *i* to *i* + 3 or *i* to *i* + 4 positions in a helix, into an HIV-1 fusion inhibitory peptide can form intramolecular E–K or K–E salt bridges that result in substantial enhancement of the peptide's stability, solubility, and antiviral activity (*30*, *31*). Using a similar design, we further optimized the sequence of OC43-HR2P by introducing Glu or Lys at appropriate sites in the peptide to increase the solubility and thereby the antiviral activity of the peptide. Moreover, on the basis of the structure of MERS-CoV S 6-HB, we also introduced mutations at some sites that are not expected to be involved in HR1 binding, such as 4Q, 14Y, 32D, and 36L, to further enhance the fusion inhibitory activity of the peptide (table S2). Among the series of optimized peptides, peptides EK0-1, EK0-2, EK0-3, and EK1 showed gradually increased solubility and excellent inhibitory activity in cell-cell fusion assays. The final peptide, EK1, exhibited the most potent pan-CoV antiviral fusion activity with IC_{50} values in the range of 0.19 to 0.62 μM (table S2). In some HCoV cell-cell fusion assays, EK1 exhibited even more effective inhibitory activity than the autologous peptide, such as MERS-HR2P and SARS-HR2P. Akin to its ancestor OC43-HR2P, EK1, which is derived from the short 6-HB fusion core of OC43, was also able to potently inhibit the cell-cell fusion mediated by 229E and NL63 S proteins, both of which harbor the long fusion core. These results further underscore the broad-spectrum anti-HCoV potential of EK1 (Fig. 2, A to E, and table S2). Furthermore, EK1 also had superior pharmaceutical properties and solubility in phosphate-buffered saline (PBS) and water, which increased by 478-fold and 3.5-fold, respectively, as compared to the original OC43-HR2P. Together, these results establish an important framework and platform for subsequent development of EK1 as a potential therapeutic (table S2).

EK1 peptide potently inhibits multiple CoV cell-cell fusion and blocks various pseudotyped and live CoV infection

SL-CoVs, including WIV1, Rs3367, and SHC014 CoVs, all manifest potential for human infection (*9*–*11*). To further assess the breadth of fusion inhibitory activity, as demonstrated by EK1, we established cell-cell fusion assays mediated by the S protein of these SL-CoVs (fig. S2). Notably, many studies have suggested diversity in the receptor-binding motif (RBM) of SL-CoV's RBD (*9*–*11*), which

Downloaded from http://advances.sciencemag.org/ on April 10, 2019

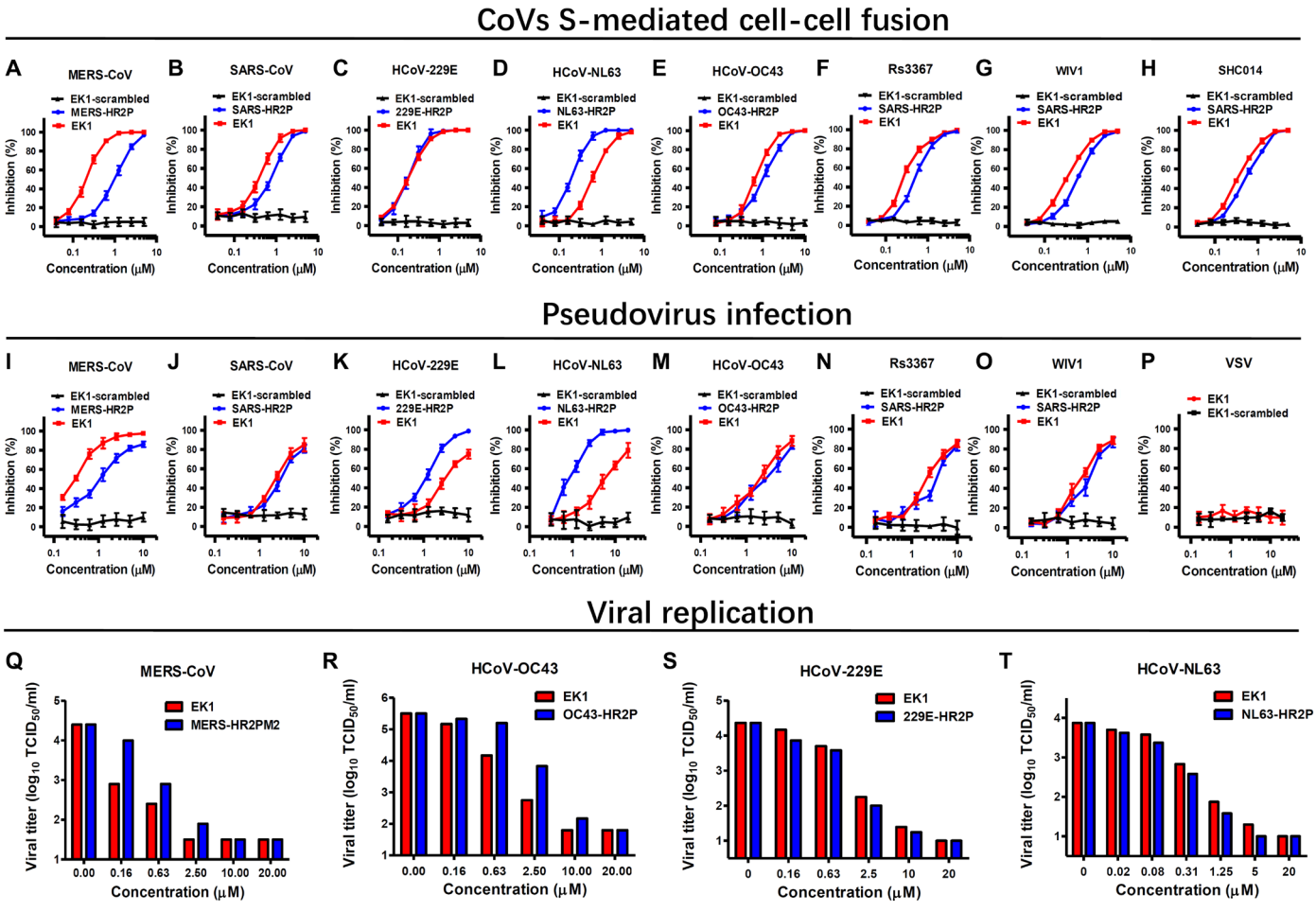

Fig. 2. EK1 is effective against viral infection mediated by S protein of multiple HCoVs. (**A** to **H**) Inhibitory activity of EK1 in cell-cell fusion mediated by the S proteins of MERS-CoV (A), SARS-CoV (B), 229E (C), NL63 (D), OC43 (E), Rs3367 (F), WIV1 (G), and SHC014 (H). (**I** to **P**) Inhibitory activity of EK1 in pseudovirus infection assays against MERS-CoV (I), SARS-CoV (J), 229E (K), NL63 (L), OC43 (M), Rs3367 (N), WIV1 (O), and VSV (P). (**Q** to **T**) Inhibitory activity of EK1 on live HCoV replication for MERS-CoV (Q), OC43 (R), 229E (S), and NL63 (T). Data are means ± SD of triplicate samples from a representative experiment.

plays an important role in binding the cellular receptor and serves as an effective target site for the development of CoV-specific antibodies or vaccines (*32*). Specifically, the RBM of SHC014 CoV has only 80% similarity and 64% identity to that of SARS-CoV, and an antibody targeting the SARS-CoV RBD could not prevent infection mediated by the SHC014 S protein (*9*–*11*, *17*). In contrast, the HR1 and HR2 sequences of SL-CoV are 100% identical to those of SARS-CoV (fig. S2B). Correspondingly, EK1 exhibited greater inhibitory activity than the autologous peptide SARS-HR2P against cell-cell fusion mediated by the S protein of the three SL-CoVs tested (Fig. 2, F to H), while an EK1-scrambled peptide showed no inhibitory activity on cell-cell fusion mediated by any of these CoV S proteins (Fig. 2, A to H).

The pseudovirus assay is a good model to mimic the process of virus entry into the target cell and has been widely used in previous studies to assess the inhibitory activity of antiviral agents against related CoV infection (*33*). We also used here pseudovirus assays to assess the inhibitory activity of EK1 against different pseudotyped HCoVs. In a MERS-CoV pseudovirus infection assay, both EK1 and MERS-HR2P showed inhibitory activity with IC_{50} values of 0.26 and 1.06 μM, respectively (Fig. 2I). Similarly, EK1 and SARS-HR2P also effectively blocked SARS-CoV pseudovirus infection with IC_{50} values of 2.23 and 2.81 μM, respectively (Fig. 2J). Meanwhile, EK1 demonstrated antiviral activity against pseudotyped 229E, NL63, and OC43 infection with IC_{50} values of 3.35, 6.02, and 1.81 μM, respectively (Fig. 2, K to M). Consistent with the results from cell-cell fusion assays, both EK1 and SARS-HR2P inhibited pseudotyped Rs3367 virus infection with IC_{50} values of 2.25 and 3.05 μM, respectively, and prevented WIV1 pseudovirus infection with IC_{50} values of 2.10 and 2.73 μM, respectively (Fig. 2, N and O). In contrast, EK1 exhibited no inhibitory activity against VSV-G–mediated viral infection (Fig. 2P). The EK1-scrambled peptide showed no inhibitory activity on infection by any of these pseudoviruses (Fig. 2, I to P). As previously reported (*10*), we failed to assemble a pseudotyped SHC014 and thus did not perform pseudovirus infection assays on this virus. Collectively, pseudovirus infection by all HCoVs and SL-CoVs could be efficiently blocked by EK1, further indicating that EK1 has broad-spectrum antiviral activity against infection by pan-HCoVs, including α-HCoVs, β-HCoVs, and SL-CoVs.

Blam-Vpr assay is a sensitive model to characterize the inhibitory mechanism and activity of antiviral agents on virus–cell membrane

Downloaded from http://advances.sciencemag.org/ on April 10, 2019

fusion. This assay has been widely used for assessing the membrane fusion activity of various viruses, including HIV-1, Ebola virus, and henipavirus (*34*–*37*). Here, we developed the Blam-Vpr assays for MERS-CoV and SARS-CoV to further clarify the fusion inhibitory mechanism of EK1. We found that EK1 effectively inhibited the entry of MERS-CoV Blam-Vpr virions and SARS-CoV Blam-Vpr virions into Huh-7 cells and ACE2-293 T cells, respectively, in a dose-dependent manner (fig. S2D), thus confirming that EK1 does act as an HCoV fusion inhibitor.

Subsequently, we further evaluated the inhibitory activity of EK1 against live HCoV infection, including MERS-CoV, OC43, 229E, and NL63. We found that EK1 could effectively inhibit the infection and replication of these HCoVs at cellular level in a dose-dependent manner (Fig. 2, Q to T). EK1 even surpassed the autologous OC43-HR2P (IC_{50} = 0.93 μM) or MERS-HR2M2 [IC_{50} = 0.23 μM; which is an optimized MERS-HR2P peptide (*33*)] against OC43 or MERS-CoV with IC_{50} values of 0.62 and 0.11 μM, respectively. Meanwhile, EK1 also exhibited equally effective inhibitory activity against 229E and NL63 infections with IC_{50} values of 0.69 and 0.48 μM, respectively, compared to 229E-HR2P (IC_{50} = 0.56 μM) and NL63-HR2P (IC_{50} = 0.14 μM) (Fig. 2, S and T). Unfortunately, because of the global prohibition of handling live SARS-CoV in most virology laboratories, we could not test the inhibitory activity of EK1 against SARS-CoV replication.

EK1 exhibits broad anti-HCoV activity in vivo

The respiratory tract is the primary target tissue of HCoV infection. To investigate the preclinical potential of the EK1 peptide, we administered it via an intranasal route and assessed its distribution within the respiratory tract. We observed the fluorescent signals of Cy5-EK1 mainly in the upper and lower respiratory tract of mice (Fig. 3, A and B). Compared with those from PBS-treated mice, the lungs obtained from Cy5-EK1–treated mice exhibited significantly higher fluorescence signals ($P < 0.0001$, $n = 3$) (Fig. 3, C and D). Together, these results suggest that EK1 (intranasal) can widely be distributed in the whole respiratory tract and be enriched in the lung. We also noted that Cy5-EK1 administered intranasally could be detected in significant amounts in several extrapulmonary organs, including the liver, kidney, and spleen, in some animals, suggesting that EK1 could enter into the blood circulation and other organs (fig. S3, A and B). This observation suggests that intranasal administration of EK1 could also be beneficial for multiorgan infection or systemic infection of HCoVs, both of which are common in MERS-CoV infection.

Next, we assessed the protective effect of EK1 in vivo on OC43 and MERS-CoV infection mouse models. In the OC43-infected mouse model, we treated newborn mice with EK1 at a dose of 5 mg/kg or with PBS 30 min before or after challenge with HCoV-OC43 at 10^2 $TCID_{50}$ (50% tissue culture infectious dose). Body weight of mice in the viral control group decreased, starting from 5 days postinfection (dpi), and mice succumbed to infection by 10 dpi with 100% mortality (Fig. 3, E to G). In contrast, the final survival rate of mice in the EK1 prophylactic and therapeutic groups was 100 and 66.7%, respectively (Fig. 3E), and their body weight either appeared normal (prophylactic) or rapidly recovered at 16 dpi (therapeutic) (Fig. 3F). Meanwhile, we tested the viral titers in brains of mice of all groups at 5 dpi. Infectious virus was readily detectable in the viral control group, whereas infectious virus titers were below the limit of detection (2 log $TCID_{50}$/g) in the EK1 prophylactic mice or very low in the EK1 therapeutic mice (Fig. 3G). However, the infectious virus titers in the brains of mice that died during EK1 therapeutic treatment were as high as those in the brains of viral control mice without EK1 treatment, while the viral titers in the brains of survival mice with EK1 therapeutic treatment and in those of normal control mice were both undetectable (fig. S2E). Consistently, the brains of mice that died during EK1 therapeutic treatment exhibited similar histopathological changes as those of the viral control mice, i.e., similar amount of vacuolation, degeneration, and infiltration (fig. S2F). In contrast, the brains of the survival mice with EK1 therapeutic treatment and those of the normal control mice showed no apparent histopathological changes (fig. S2F).

To evaluate the prophylactic and therapeutic potentials of EK1 against MERS-CoV infection, we took advantage of the well-characterized transgenic (Tg) mice globally expressing human dipeptidyl peptidase IV (DPP4) viral receptor. We treated mice with 200 μg of EK1 or with PBS 30 min before or after challenge with MERS-CoV at 10^4 $TCID_{50}$. Likewise, the weight loss of Tg mice treated with EK1 before or after MERS-CoV challenge was insignificant and rapidly recovered at 16 dpi, while untreated mice progressively lost significant weight before succumbing to infection within 9 dpi with 100% mortality (Fig. 3, H to J). In contrast, the survival rates in the EK1 prophylactic and therapeutic groups were 100 and 75%, respectively (Fig. 3, H to J). When the yield of infectious viruses in lungs was used as the end point for assessing the efficacy of EK-1 on MERS-CoV infection, we were unable to recover any infectious virus from both EK1 prophylactic and therapeutic groups, in sharp contrast to the untreated controls (Fig. 3J). Together, these results indicated that the peptide EK1 has broad and potent prophylactic and therapeutic efficacy against HCoV infections.

The safety and low immunogenicity of EK1

Safety is obviously very important for the development of EK1 in clinical applications, and therefore, we first tested its in vitro cytotoxicity on various target cells. EK1 is not cytotoxic at concentrations up to 1 mM, which is more than 200 times higher than its IC_{50} for inhibiting any HCoV S-mediated cell-cell fusion and pseudovirus entry (fig. S3C). We then further investigated its cytotoxicity in vivo. We continuously administered mice with PBS, low-dose EK1 (20 mg/kg), or high-dose EK1 (100 mg/kg) by intranasal route every day for 1 week, and we recorded the body weight changes for the following 2 weeks (fig. S3D). The EK1-treated mice in both high- and low-dose groups lived normally, with no apparent difference in weight gain/loss observed as compared to PBS-treated mice. Meanwhile, we used enzyme-linked immunosorbent assay (ELISA) to measure EK1-specific antibodies in sera of mice 2 weeks after intranasal administration. No EK1-specific antibodies were detected in either the EK1-treated group or in the PBS-treated group (fig. S3E).

On the basis of the distribution of EK1 by intranasal administration (fig. S3, A and B), we postulated that EK1 could penetrate the air-blood barrier to enter blood circulation and become enriched in some important organs, such as the liver and kidney. Therefore, we further examined levels of alanine aminotransferase (ALT; fig. S3F) and creatinine (fig. S3G) in the sera of mice. ALT and creatinine showed no significant difference ($P > 0.05$) at all time points between EK1- and PBS-treated groups, suggesting that nasal application of EK1 at high or low doses did not affect mouse hepatic and renal function.

We further compared the potential histopathological changes of EK1- and PBS-treated groups 4 weeks after administration. The

Downloaded from http://advances.sciencemag.org/ on April 10, 2019

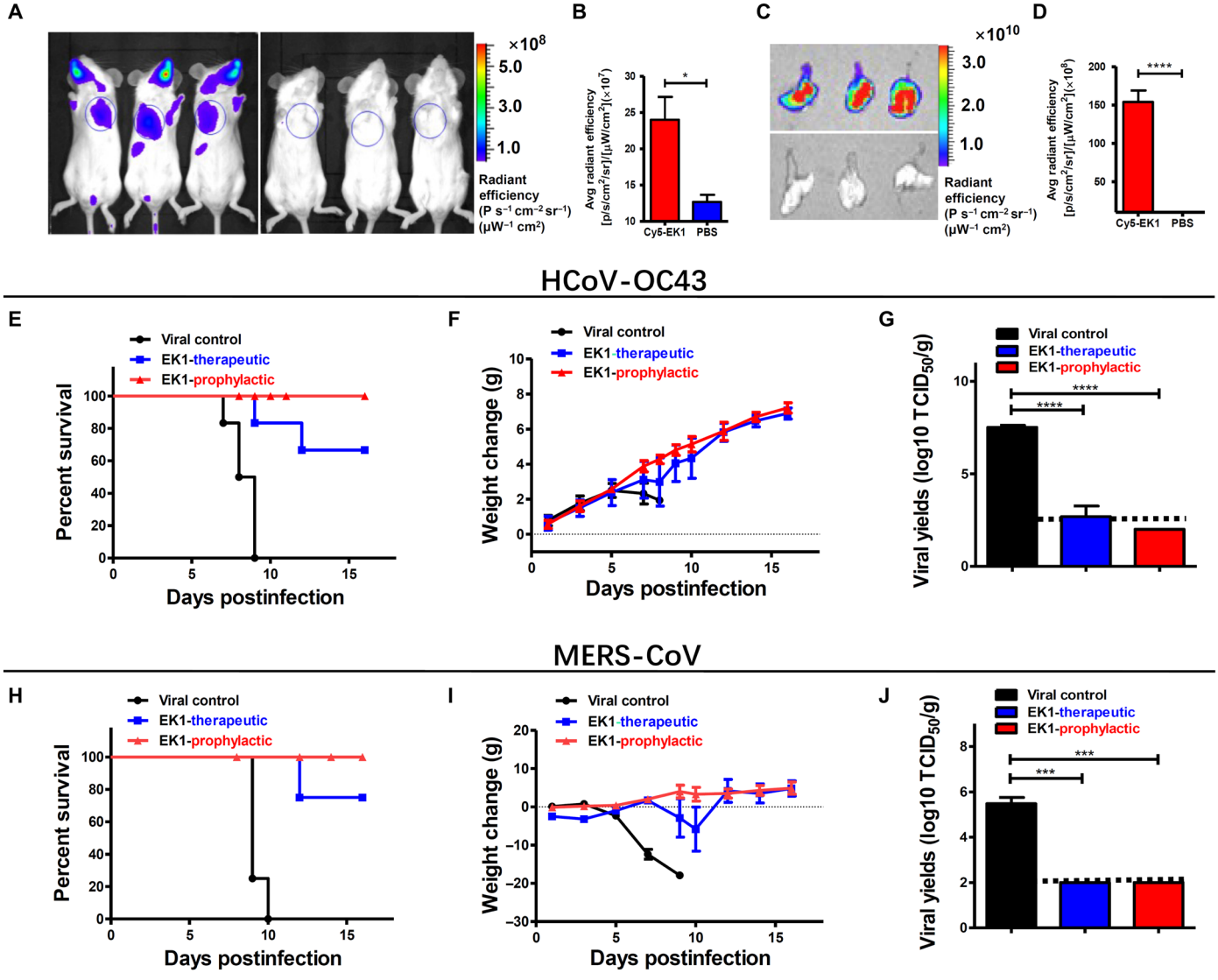

Fig. 3. In vivo prophylactic and therapeutic efficacy of EK1 in mice against OC43 and MERS-CoV infection. (**A** and **B**) Imaging of mice treated with Cy5-EK1 or PBS by the IVIS Lumina K Series III from PerkinElmer and the statistical analysis. (**C** and **D**) Imaging of lungs from those mice with the statistical analysis. (**E** to **G**) Anti–OC43 efficacy of EK1 in vivo. Survival curves of 3-day-old suckling mice challenged with OC43. (E) Newborn mice were treated with EK1 (5 mg/kg in PBS) or PBS 30 min before or after challenge with OC43 (10^2 $TCID_{50}$). (F) Body weight change of newborn mice treated with EK1 or PBS 30 min before and after OC43 challenge. (G) Viral titer in mouse brain of each group. (**H** to **J**) Anti–MERS-CoV efficacy of EK1 in vivo. Survival curves of mice challenged with MERS-CoV. (H) Mice expressing human DPP4 were treated with 200 μg EK1 in PBS or PBS 30 min before or after challenge with MERS-CoV (10^4 $TCID_{50}$). (I) Body weight change of each group of mice. (J) Viral titer in mouse lungs of each group. SD of triplicate samples from a representative experiment; *$P < 0.05$, ***$P < 0.001$, and ****$P < 0.0001$.

hematoxylin and eosin staining of lung, liver, kidney, and spleen sections from mice treated with EK1 at different doses exhibited no pathological abnormality, when compared to control mice treated with PBS (fig. S3H). None of these organs showed evidence of cell degeneration, necrosis, or infiltration of inflammatory factors. Hence, EK1 appears to be generally safe via nasal application.

Structural basis of EK1 pan-CoV inhibitory activity

To investigate the structural basis for the pan-CoV inhibitory effect of EK1 peptide, we crystallized EK1 in complex with HR1 peptides from three representative HCoVs, including the most pathogenic SARS-CoV and MERS-CoV in β-HCoVs and 229E in α-HCoVs, the HR1 of which is 14 amino acids longer than those of β-HCoVs.

Crystal structures of HR1(MERS)-L6-EK1, HR1(SARS)-L6-EK1, and HR1(229E)-L6-EK1 were solved by molecular replacement and refined to final resolutions of 3.3, 3.3, and 2.2 Å, respectively (table S3). In all three structures, EK1 snugly fits into the hydrophobic groove formed between two adjacent HR1 helices in an oblique and antiparallel manner (Fig. 4, A to C), producing a 6-HB structure resembling the 3HR1-3HR2 postfusion state of corresponding HCoVs (fig. S4). Notably, the binding sites of EK1 coincide with those of native HR2s (fig. S4). These results indicate that the presence of EK1 would preclude binding of HR2 onto their corresponding 3HR1 core, thereby blocking formation of the 3HR1-3HR2 6-HB, which is an indispensable step during host-viral membrane fusion. Hence, administration of the EK1 peptide would block cellular entry of those HCoVs (Fig. 2).

Downloaded from http://advances.sciencemag.org/ on April 10, 2019

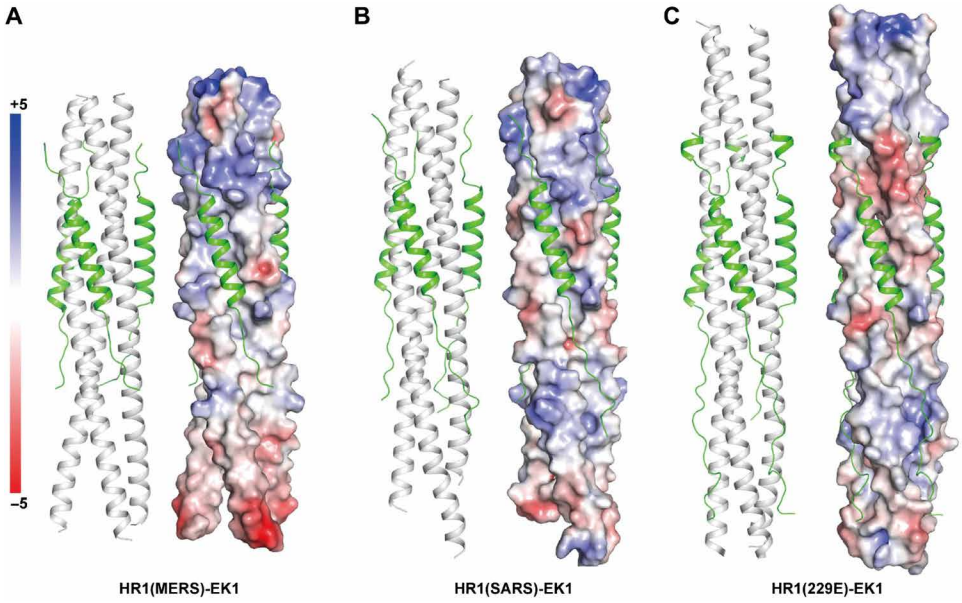

Fig. 4. Interaction of EK1 with HCoV. Side-by-side ribbon diagram and electrostatic surface representations illustrate that EK1 snugly fits into the hydrophobic groves formed between two adjacent HR1 helices of the 3HR1 core from MERS-CoV (**A**), SARS-CoV (**B**), and 229E (**C**). The EK1 peptide is shown as a green on white ribbon (left) and electrostatic (right) representations of corresponding HCoV 3HR1 cores. Hydrophobic surfaces are in whitish gray, basic in blue, and acidic in red.

In all three structures, the EK1 peptide adopts a mixed secondary structure conformation (Fig. 4, A to C). The central region of EK1 folds into a five-turn helix, which packs against two neighboring HR1 helices via extensive hydrophobic interactions (3HR1 cores of different HCoVs are illustrated as electrostatic surfaces, while residues on EK1 that are involved in hydrophobic packing are shown as stick models; residues L12, E15, M16, L19, A22, I23, L26, S29, and Y30 on EK1 locate within the five-turn helix of EK1 and form strong hydrophobic interactions with the 3HR1 cores; Fig. 5A) and a few electrostatic or polar interactions (residues E13, E15, K18, E20, E27, E28, and Y30 locate within the five-turn helix region of EK1 and interact with HR1 residues through side chain–to–side chain hydrophilic interactions; Fig. 6A). The rest of EK1 adopts an extended conformation, except that one extra turn is formed at the C-terminal end of EK1 (around E35) in the HR1(229E)-L6-EK1 structure (Fig. 6, right panel). In the extended region of EK1, polar interactions between side chain (HR1 residues) and main chain (EK1 residues) dominate (compare Fig. 6, B and A). Most of these side chain–to–main chain polar interactions cluster at either end of the EK1 helical region, which interweave into extensive H-bond networks and likely help secure the EK1 helical region in the correct register (Fig. 6B). Hydrophobic residues in the extended region of EK1 also insert their bulky side chains into hydrophobic pockets on the surface of the 3HR1 cores (residues L2, I5, V7, L10, I31, and L36; Fig. 5A), further strengthening the adhesion of the EK1 extended region onto the 3HR1 cores.

Both hydrophobic pockets and ridges exist on the surface of 3HR1 cores (Fig. 5A). Correspondingly, we observed two kinds of hydrophobic interactions between the EK1 and 3HR1 cores. In particular, certain EK1 residues insert their hydrophobic side chains into pockets on the 3HR1 cores (Fig. 5A, shown as orange stick models and hereafter named as "burying residues"), and other EK1 residues pack their side chains against hydrophobic ridges on the 3HR1 cores (Fig. 5A, shown as yellow stick models and hereafter named as "ridge-packing residues"). Note that the residues on HR1 that mediate hydrophobic interactions with the burying and ridge-packing residues on EK1 are conserved across all HCoVs [Fig. 5B (bottom panel), HR1 residues shaded with orange and yellow], and most of the HR1 residues involved in polar and electrostatic interactions with EK1 also manifest high levels of similarity across all HCoVs [Fig. 5B (bottom panel), HR1 residues boxed in cyan and red]. Thus, EK1 would be able to form similar hydrophobic and hydrophilic interactions with HR1s from OC43, HKU1, and NL63, as we observed in the homology models of HR1(OC43)-L6-EK1, HR1(HKU1)-L6-EK1, and HR1(NL63)-L6-EK1 (fig. S5). Together, extensive and highly conserved hydrophobic and hydrophilic interactions between EK1 and 3HR1 cores endow EK1 with the ability to bind the 3HR1 cores from different HCoVs and, hence, the capability of blocking the association of different HR2s onto their corresponding 3HR1 cores (Fig. 2).

The EK1 peptide outcompetes self-derived HR2 of MERS-CoV in both cell-cell fusion and pseudovirus infection assays. We therefore also compared the interactions between EK1 and MERS-HR1 (Figs. 5A and 6, left panel) with those between MERS-HR2 and MERS-HR1 (fig. S6A). Most hydrophobic interactions between EK1 and MERS-HR1 are similar to those between MERS-HR2 and MERS-HR1 [compare Fig. 5A (left panel) and fig. S6A (left panel)]. Nevertheless, EK1 formed more side chain–to–side chain hydrophilic interactions with MERS-HR1 [compare Fig. 6A (left panel) and fig. S6A (middle panel)] than did MERS-HR2, which likely accounts for its better IC_{50} in cell-cell fusion and pseudovirus infection assays (Fig. 2).

Similar to HR1 from α-HCoVs, sequence alignment across HCoVs revealed that a 14–amino acid insertion also exists in the HR2 region of α-HCoVs (Fig. 1C). Such an insertion renders the HR2 helices of α-HCoVs four turns longer than those of β-HCoVs. The helical region of EK1 is only five turns long, much shorter than the nine-turn helix in 229E-HR2 (*38*). Nevertheless, the burying residues in the extended region of EK1 and their equivalents in 229E-HR2 all neatly insert their side chains into corresponding

Downloaded from http://advances.sciencemag.org/ on April 10, 2019

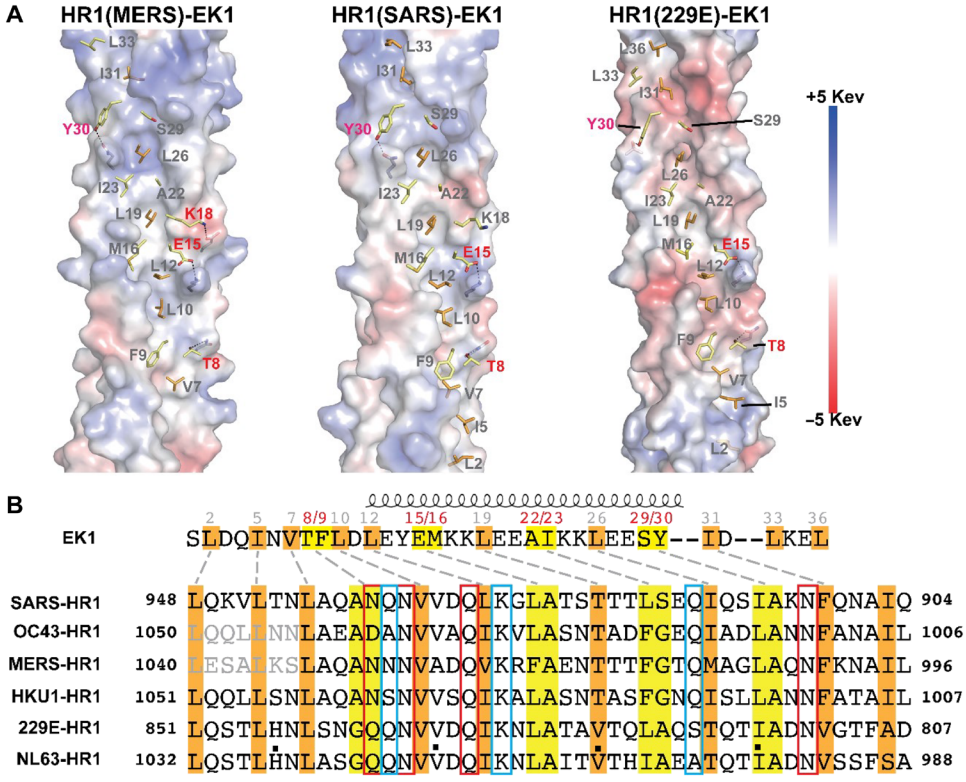

Fig. 5. Hydrophobic packing between EK1 and 3HR1 hydrophobic cores are largely conserved across different EK1-HR1 complexes. (**A**) The 3HR1 cores are shown as electrostatic surfaces. At the positions where the hydrophobic surface on the 3HR1 core is deeply concave (pockets), EK1 residues that bury over 70% of their side-chain solvent accessible surface (SAS) into these pockets are shown as orange stick models. At the locations where the hydrophobic surface on the 3HR1 core is relatively flat (ridges), EK1 residues that pack 50 to 70% of their side-chain SAS against these ridges are shown as light yellow stick models. EK1 residues are labeled, where those labeled in red form both hydrophobic and hydrophilic interactions with 3HR1 cores. (**B**) HR1 residues involved in interactions with EK1 are conserved across different HCoVs. EK1 and HR1 residues linked with dashed lines locate to the same layers on the 3HR1 triple helix. Burying EK1 residues are shaded orange, and ridge-packing EK1 residues are shaded light yellow. HR1 residues that mediate assembly of the 3HR1 cores are shaded orange, while those involved in ridge packing are shaded yellow. HR1 residues that mediate conserved side chain–to–side chain and side chain–to–main chain hydrophilic interactions with EK1 residues are highlighted with cyan and red boxes, respectively.

hydrophobic pockets (fig. S6C), although these residues are located in extended regions in EK1, while their equivalents are within α-helical regions in 229E-HR2 (fig. S6C). As a consequence, the hydrophobic interactions between EK1 and 229E-HR1 are not compromised at all in comparison to those between 229E-HR2 and 229E-HR1 [compare Fig. 5A (right panel) and fig. S6B (left panel)]. Furthermore, a total of 12 polar and electrostatic interactions occur between EK1 and 229E-HR1, including five side chain–to–side chain and seven side chain–to–main chain interactions [Fig. 6, A and B (right panel)]. Together, these extensive hydrophobic and hydrophilic interactions preserve the high affinity of EK1 toward long HR1 HCoVs. That EK1 can form 6-HB structures with both short (SARS-CoV and MERS-CoV) and long (229E) HR1s highlights its broad structural compatibility in accommodating HR1s from different HCoVs, thus consolidating its broad-spectrum inhibitory effect against pan-CoVs.

DISCUSSION

No effective and broad-spectrum anti-HCoVs drugs or vaccines are currently available in the clinic. Notwithstanding, the RBD of the S protein has been proposed as a promising target for the development of specific antibodies and vaccines (*39*, *40*). For example, the RBD-specific antibody CDC2-C2 exhibits inhibitory activity against MERS-CoV infection. Nevertheless, administration of the single-antibody CDC2-C2 could result in the emergence of escape mutations in MERS-CoV RBD (*41*). Unfortunately, the CoV S RBD is hypervariable throughout evolution, which has led to marked difference in host receptor usage in different HCoVs. Even when the same host receptor is used by different HCoVs, they frequently target different binding sites on the host receptor (*42*). Therefore, specific RBD-targeting antibodies or vaccines inevitably lack broad-spectrum activity against HCoV infection. For example, Menachery *et al.* (*9*) found that a SARS-CoV RBD-specific antibody could not protect mice from infection by the chimeric virus with the SHC014 S proteins, although SHC014 has high homology with SARS-CoV and can bind the same host receptor ACE2. The lag time between emerging human CoV outbreaks and development of new prophylactic treatments or vaccines is of concern. Thus, there is an urgent need for the development of new, broad-spectrum drugs that target conserved sites in currently circulating and future emerging HCoVs so as to prepare for future outbreaks of yet unknown HCoVs.

Downloaded from http://advances.sciencemag.org/ on April 10, 2019

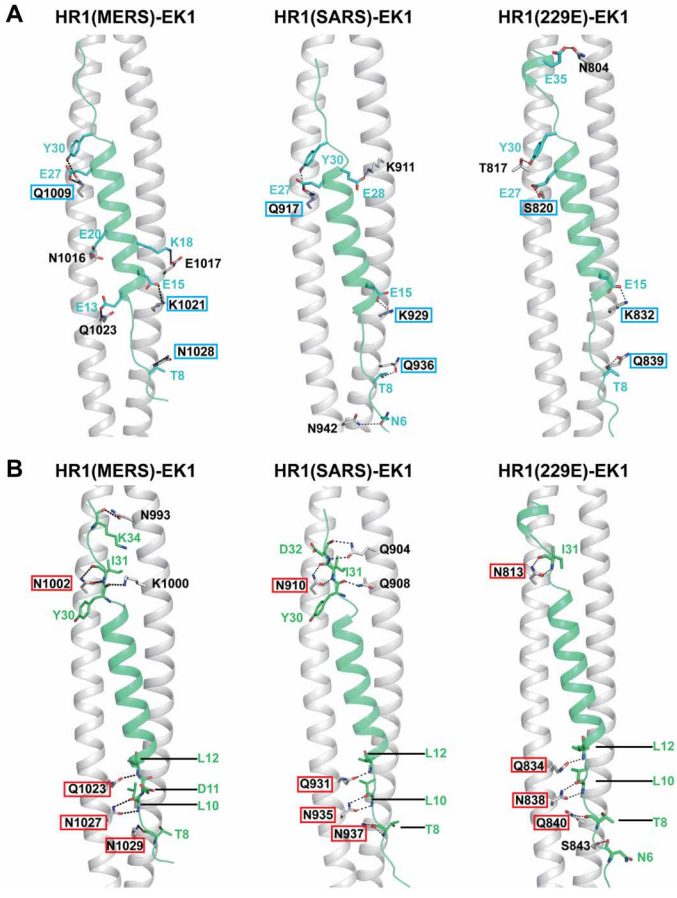

Fig. 6. Highly conserved hydrophilic interactions between EK1 and 3HR1 cores. (**A**) Side chain–to–side chain hydrophilic interactions between EK1 and HR1. Side chains of EK1 and HR1 residues involved in these interactions are shown as cyan and gray stick models, respectively, and are similarly color-coded. At least four pairs of this hydrophilic interaction are conserved across different EK1-HR1 complexes: $Y30^{EK1}$ forms similar polar interactions with $Q1009^{MERS}$ (left), $Q917^{SARS}$ (middle), or $T817^{229E}$ (right); $E27^{EK1}$ forms similar polar interactions with $Q1009^{MERS}$ (left), $Q917^{SARS}$ (middle), or $S820^{229E}$ (right); $E15^{EK1}$ forms salt bridges with $K1021^{MERS}$ (left), $K929^{SARS}$ (middle), or $K832^{229E}$ (right); and $T8^{EK1}$ makes similar interactions with $N1028^{MERS}$ (left), $Q936^{SARS}$ (middle), or $Q839^{229E}$ (right). The conserved HR1 residues mentioned above are highlighted with cyan boxes. (**B**) Main chain–to–side chain hydrophilic interactions between EK1 and HR1. EK1 and HR1 residues involved in these interactions are shown as green and gray stick models, respectively. The main-chain atoms of HR1 residues are not shown for clarity. Similar to the side chain–to–side chain interactions, main chain–to–side chain interactions are also highly conserved across different EK1-HR1 complexes. The HR1 residues involved in conserved interactions are highlighted with red boxes.

In the early 1990s, a series of peptides derived from the HIV-1 gp41 HR2 (or CHR) domain, such as SJ-2176 (*19*), DP-178 (later T20) (*20*), and C34 (*21*), were reported to have highly potent inhibitory activity against HIV-1 gp41-mediated membrane fusion and HIV-1 infection with IC_{50} values at low nanomolar levels. Subsequently, numerous virus fusion inhibitory peptides overlapping the HR2 sequences of class I membrane fusion proteins from other enveloped viruses, including RSV (*22*), Ebola virus (*23*), paramyxoviruses SV5 (*24*), and Nipah virus (*25*), were also reported. In 2003, Bosch *et al.* (*26*) discovered that a soluble HR2 peptide derived from the MHV S protein HR2 region inhibited virus cell entry, suggesting that the S glycoprotein of CoV is a class I fusogen with the ability to form 6-HB during the S protein–mediated membrane fusion process. In 2004, the Bosch (*43*) and Jiang (*18*) groups independently reported that peptides derived from the HR2 region of SARS-CoV S protein could interact with the peptides from its HR1 region to form 6-HB and inhibited SARS-CoV S protein–mediated membrane fusion and SARS-CoV infection with moderate potency. In 2014, Lu *et al.* (*27*) reported that peptide derived from the MERS-CoV S-HR2 could competitively inhibit 6-HB formation, thereby preventing fusion of the virus with host cells.

In our previous studies, we found that the MERS-CoV–specific fusion inhibitor MERS-HR2P could not block SARS-CoV pseudovirus infection and did not display any broad-spectrum inhibitory activity. Thus, it was unclear whether 6-HB was a good target site for the development of a broad-spectrum anti-HCoV inhibitor. To identify a pan-HCoV fusion inhibition target site and preferably also to develop a potential pan-HCoV inhibitor against infection of multiple HCoVs in the human respiratory tract, we successfully established multiple HCoV S-mediated cell-cell fusion assays to determine the cross-inhibitory spectrum between HR1Ps and HR2Ps, which are derived from the HR1 and HR2, respectively, of HCoVs. Unexpectedly, we found that OC43-HR2P harbored broad-spectrum binding activity to all HR1Ps and manifested fusion inhibitory activity against all HCoV S-mediated cell-cell fusion. We then further optimized the OC43-HR2P to improve its antiviral activity and solubility. The optimized peptide EK1 exhibited broad and potent fusion inhibitory activity against infection by HCoVs and SL-CoVs on various in vitro models, i.e., cell-cell fusion assays and pseudotyped or live viral infection assays. We assessed the prophylactic and protective effects of EK1 through intranasal administration on OC43 and MERS-CoV mouse models. EK1 exhibited effective preventive and protective effects in these mouse models with an acceptable in vivo safety profile. Furthermore, the in vivo pharmacokinetic profiling and safety studies helped us acquire useful data for potential human clinical trials in the future.

The potency of HR2-derived peptides in inhibiting corresponding virus-cell fusion varies significantly. For example, anti–HIV-1 peptide T20 is about 900-fold more potent than the anti–SARS-CoV peptide SC-1, yet only 30-fold more potent than the anti–MERS-CoV peptide HR2P (*18*, *27*, *44*). It is known that HIV-1 and SARS-CoV each enter their target cells mainly through plasma and endosomal membrane fusion, respectively, while MERS-CoV could infect its target cells via both plasma and endosomal membrane fusion (*18*, *27*, *44*). The vast differences seen in potency thus suggest that only a limited number of the EK1 peptides can get into the endosome to inhibit virus-cell fusion. Therefore, increasing the cell permeability of the fusion inhibitory peptides is expected to enhance the potency of these peptides. We have recently reported that addition of hydrocarbon stapling or a palmitic acid group (C16) to the MERS-CoV fusion inhibitory peptides significantly improves their antiviral potency and pharmacokinetic properties (*45*, *46*). In the near future, we will use the similar approaches to improving the antiviral activity of EK1.

Recent studies have reported that several emerging SL-CoVs, including WIV1, SHC014, and Rs3367, have the potential to infect humans with high virulence by further evolution or direct gene recombination with SARS-CoV (*9*, *11*). We found that the HR sequences of these SL-CoVs are the same as those of SARS-CoV, and we predicted that EK1 could prevent infection by these SL-CoVs. As

Downloaded from http://advances.sciencemag.org/ on April 10, 2019

expected, EK1 efficiently inhibited SL-CoV S protein–mediated cell-cell fusion. Consistent with previous studies (*9*, *11*), we herein also failed to establish a SHC014 pseudovirus using an HIV-1 backbone vector; therefore, we assessed the antiviral effect of EK1 only on WIV1 and Rs3367 pseudovirus infection and found that EK1 exhibited effective inhibitory activity against these two SL-CoVs. In addition, some animal CoVs within the CoV family are very close to HCoV, such as bovine coronavirus (BCoV) and MHV. The HR sequences of these CoVs are very similar to those of OC43, indicating that peptide EK1 will likely also be effective on these viruses.

One intriguing question is why only EK1 and the HR2 from OC43 manifested "pan-CoV" inhibitory activity, while HR2 from other HCoVs did not. HR2s from α-HCoVs are substantially longer than those from β-HCoVs (Fig. 1C), and docking of HR2s from 229E and NL63 onto the 3HR1 cores of β-HCoVs resulted in severe steric clashes (figure not shown). It is thus understandable why the HR2s from 229E and NL63 would not have broad-spectrum activity toward β-HCoVs (Fig. 1D).

At the same time, sequence alignment between EK1 and HR2s from OC43, SARS-CoV, and MERS-CoV provided clues on the very limited inhibition breadth of SARS-HR2 and MERS-HR2. Although most residues that mediated hydrophobic (shaded orange and yellow) and side chain–to–side chain hydrophilic interactions (boxed in cyan) are conserved between EK1 and different HR2s, sequence variability does exist at positions V7, Y30, and some other ridge-packing residues (fig. S7A). We thus focused our analysis on these residues and their surrounding environments in different HCoVs' 3HR1 cores. In both solved structures of MERS(HR1)-EK1 and SARS(HR1)-EK1, $V7^{EK1}$ fits its side chain neatly into the hydrophobic pockets on these two 3HR1 cores (fig. S7B, second and fourth panels). Nevertheless, in the previously reported structure of the SARS-CoV fusion core, $A1156^{SARS}$, the equivalent of $V7^{EK1}$ in SARS-CoV, would occupy the same cavity loosely (fig. S7B, third panel), while $T1257^{MERS}$, the equivalent of $V7^{EK1}$ in MERS-CoV, could not fully bury its side chain owing to the polar nature of the Thr residue (fig. S7B, first panel). Thus, Val, in EK1 and OC43-HR2, is more effective in fitting the hydrophobic cavities at this position than Ala (seen in SARS-HR2) or Thr (seen in MERS-HR2) (fig. S7B).

In total, we observed four ridge-packing interactions between the EK1 and 3HR1 cores. The ridge to which $S29Y30^{EK1}$ binds is surrounded by polar and positively charged residues in MERS-CoV and SARS-CoV but surrounded by polar and negatively charged residues in 229E [fig. S7C (top panel), side chains of surrounding residues are shown as stick models]. At this position, the polar pair "Ser-Tyr" in EK1 and OC43-HR2 appears to be more suitable than the "Ser-Leu" pair from SARS-HR2 in accommodating the opposite electrostatic environments in different HCoVs. Moreover, the aromatic ring of Tyr could also form additional polar interactions with HR1 side chains in different HCoVs (Fig. 6A). Likewise, the ridges to which $E15M16^{EK1}$ binds also exhibited better shape complementarity to Met (in EK1 and OC43-HR2) than to Ile (in SARS-HR2). Collectively, it seems that EK1 and OC43-HR2 have more optimal amino acid choices at all the abovementioned critical positions, which likely accounts for their unique pan-CoV inhibitory activity.

In its natural state, the S protein that is present on the CoV surface is inactive. After receptor binding target cell proteases activate the S protein by cleaving the exposed enzyme target sites, leaving the S2 subunit free to mediate viral fusion and entry. CoV can enter the target cell via two pathways: one is the endocytosis pathway and the other is direct fusion on the cellular surface. For example, when SARS-CoV enters the target cell through the endocytosis pathway, its S protein can be cleaved and activated by the pH-dependent cysteine protease cathepsin L in the endosome. On the other hand, recent studies have consistently reported that the SARS-CoV S protein can also be cleaved and activated by transmembrane protease serine 2 (TMPRSS2) and human airway trypsin-like protease, which are located on the cell surface, thus activating and allowing the S protein to mediate SARS-CoV infection at the plasma membrane (*9*–*11*). In accord with such a finding, Matsuyama *et al.* (*47*) reported that the HR2 peptide efficiently inhibited SARS-CoV entry into cells, while lysosome-tropic reagents failed to inhibit at all. Similarly, TMPRSS2 also has the capacity to promote the entry of MERS-CoV through bypassing the endocytosis pathway and directly activating its S protein on the cellular surface (*48*). Recently, several studies have reported that TMPRSS2 is highly expressed on human respiratory epithelial cells surface and was even associated with several CoV receptors, such as ACE2 and DPP4 (*48*–*50*). Hence, the plasma membrane fusion pathway seems a preferred choice for HCoV infection in the human respiratory tract. Consistently, our previous study found that MERS-CoV–specific fusion inhibitor HR2PM2 effectively inhibited MERS-CoV infection in vivo by intranasal administration (*33*). Other studies have also reported that the current clinical isolates of 229E and OC43 are very sensitive to cell surface TMRRSS2 but not to endosomal cathepsins (*51*, *52*). Overall, for current circulating HCoVs or emerging HCoVs, the cell surface fusion pathway in human respiratory tract would appear to be very important. Therefore, peptide fusion inhibitors and the strategy of intranasal administration are excellent choices for preventing HCoV infection via the airway, which is a key site for HCoV to rapidly establish infection and widely spread to other organs.

Currently, circulating HCoVs pose a potential threat to humans; moreover, it is almost certain that other zoonotic CoVs will be transmitted to humans in the future. The availability of HCoV-specific drugs with broad-spectrum inhibitory activity is therefore important for the prevention and control of a future HCoV epidemic. The EK1 fusion inhibitor peptide targeting the conserved site in the spike HR1, but not the hypervariable RBD region, has potent and broad inhibitory activity against multiple HCoV infections. EK1 through nasal administration exhibited effective and broadly anti-HCoV activity with a satisfactory safety profile in vivo. Hence, EK1 is a promising candidate for further development as an antiviral agent against infection of multiple HCoVs, especially for use in infants and the elderly, as well as immunocompromised patients, who would be more vulnerable to HCoV infections (*53*–*56*). Meanwhile, this study provides clues and methods for the development of peptide fusion inhibitors with potency and breadth in inhibiting infections by other highly pathogenic enveloped viruses with class I membrane fusion proteins, such as Ebola and Marburg viruses, Hendra and Nipah viruses, and influenza viruses.

MATERIALS AND METHODS

Cells, viruses, and peptides

Cell lines Huh-7, Vero E6, HCT-8, Calu-3, A549, LLC-MK2, 293 T, and 293 T/ACE2 were obtained from American Type Culture Collection (ATCC; Manassas, VA, USA). All cell lines were cultured in Dulbecco's modified Eagle's medium (DMEM) with 10% fetal bovine serum (FBS). The HCoV-OC43 (VR-1558) and HCoV-229E

Downloaded from http://advances.sciencemag.org/ on April 10, 2019

(VR-740) strains were obtained from the ATCC. MERS-CoV-EMC/2012 was originally provided by H. Feldmann (National Institutes of Health, National Institute of Allergy and Infectious Diseases, Rocky Mountain Laboratories, Hamilton, MT) and R. A. Fouchier (Erasmus Medical Center, Rotterdam, Netherlands). PMD2.G-VSV-G, pcDNA3.1-MERS-S, pcDNA3.1-SARS-S, pcDNA3.1-WIV1-S, pcDNA3.1-Rs3367-S, pcDNA3.1-SHC014-S, pNL4-3.Luc.R-E, and pAAV-IRES-EGFP plasmids and the NL63 strain (Amsterdam) were preserved in our laboratory. The DNA sequence of the S protein of OC43 with a deletion of 17 amino acids in the C terminus was synthesized. DNA encoding 229E-S or NL63-S-18 (containing a C-terminal 18–amino acid deletion) was provided by F. Li. All peptides were synthesized by KareBay Biochem with a purity of >95% (tested by high-performance liquid chromatography). The EK1-scrambled sequence was "LKVLLYEEFKLLESLIMEILEYQKDSDIKENAEDTK."

CoV phylogenetic analysis

Phylogenetic trees were constructed using the MEGA6.06. Accession numbers used for phylogenetic analysis are as follows: BCoV (KX982264.1), PEDV (NC_003436), HCoV-229E (AAK32191.1), HCoV-NL63 (AVA26873.1), MHV (AC_000192.1), IBV (KY421672), HCoV-OC43 (CAA83661.1), HCoV-HKU1 (DQ415904), BtCoV-HKU4 (NC_009019.1), BtCoV-HKU5 (NC_009020), SW1 (EU111742.1), MERS-CoV (AID55097.1), SARS-CoV (ABD72979.1), BtSCoV-SHC014 (KC881005), BtSCoV-Rs3367 (KC881006), BtSCoV-WIV1 (KF367457), BtCoV-HKU9 (EF065516), HKU11 (FJ376620), HKU12 (NC_011549.1), HKU13 (NC_011550.1), and PDCoV (KX022605.1).

Expression and purification of fusion protein HR1-L6-EK1

The coding sequence of EK1 peptide was individually fused to the 3′ end of the HR1 domain from SARS-CoV, MERS-CoV, and HCoV-229E (residues 892 to 970, 984 to 1062, and 785 to 873, respectively) through a six–amino acid linker (L6: SGGRGG). The resulting sequences encoding different HR1-L6-EK1 fusion proteins were then subcloned into a modified pET-28a vector, which contains a His_6-SUMO tag upstream of the multiple cloning site. The resulting constructs, pET-28a- His_6-SUMO-HR1-L6-EK1, were then expressed in *Escherichia coli* BL21 (DE3) at 16°C overnight in LB medium. We initially purified these fusion proteins using His-Talon resin (Clontech). Eluted fractions from the His-Talon column were then mixed with Ulp1 enzyme [1:100 (w/w)] and dialyzed against buffer A [20 mM tris-HCl (pH 8.0), 150 mM NaCl, and 1 mM dithiothreitol] at 4°C overnight. After SUMO tag cleavage, the samples were reloaded onto the His-Talon column, and flow-through fractions containing untagged HR1-L6-EK1 were pooled, concentrated, and gel-filtered in buffer B [20 mM tris (pH 8.0) and 150 mM NaCl] on a HiLoad 16/60 Superdex 75 (GE Healthcare) column. Peak fractions that contain HR1-L6-EK1 trimer were pooled and concentrated to 10 mg/ml through centrifugation (EMD Millipore).

Crystallization and structure determination

Initial crystallization conditions were screened using the sitting-drop vapor diffusion method on a Mosquito crystallization robot (TTP Labtech) at 20°C. Diffraction-quality crystals of the HR1(SARS)-L6-EK1 fusion protein were obtained using the hanging-drop vapor diffusion method by mixing equal volumes (0.5 μl) of protein solution (5 mg/ml) and reservoir solution [0.2 M Li_2SO_4, 0.1 M bis-tris (pH 5.5), and 25% PEG3350]. Diffraction-quality crystals of the HR1(MERS)-L6-EK1 and HR1(229E)-L6-EK1 fusion proteins were obtained through similar methods from 0.2 M KSCN (pH 7.0), 20% PEG3350, and 0.05 M $MgCl_2$ and 0.1 M HEPES (pH 7.5) and 30% PEG550MME, respectively. Diffraction data were collected at beamline BL19U1 of Shanghai Synchrotron Radiation Facility (SSRF), China, and processed with the HKL3000 program (*57*). A summary of the data collection statistics is provided in table S3. The structure of HR1(SARS)-L6-EK1 was solved by molecular replacement, as implemented in the PHASER program of PHENIX (*58*). The programs used a SARS-CoV fusion core structure [Protein Data Bank (PDB): 2bez] as the search model. For structure determination of HR1 (MERS)-L6-EK1 and HR1(229E)-L6-EK1, the MERS-CoV fusion core [PDB: 4mod] and SARS-CoV fusion core [PDB: 2bez] were used as search models. The structural models were further improved by cycles of manual building and refinement using the COOT (*59*) and PHENIX (*58*) programs. The quality of these models were analyzed with MolProbity (*60*). A summary of the structure refinement statistics is also given in table S3. The figures were all prepared using the PyMOL program (The PyMOL Molecular Graphics System, Version 2.1, Schrödinger LLC). The electrostatic calculations were performed with PDB2PQR (*61*).

Homology model building

Models for HR1(OC43)-L6-EK1, HR1(HKU1)-L6-EK1, and HR1(NL63)-L6-EK1 were derived by homology modeling using Swiss Model website (*62*). The template for HR1(OC43)-L6-EK1 and HR1(HKU1)-L6-EK1 were obtained from the crystal structures of HR1(SARS)-L6-EK1 and HR1(MERS)-L6-EK1, and the template for HR1(NL63)-L6-EK1 proteins was obtained from the crystal structure of HR1(229E)-L6-EK1. To relax and stabilize the interaction between EK1 and corresponding HR1, initial models were optimized by performing energy minimization, followed by a 5-ns molecular dynamics simulation using Schrödinger Suite 2017-4 (www.schrodinger.com). The simulation systems were solvated with full-atom TIP3P water, containing Cl^- and Na^+ ions at a concentration of 0.15 M to mimic physiological ionic strength. During the simulation, temperature T and pressure P were kept constant, at 310 K and 1 atm, respectively.

Circular dichroism spectroscopic analysis

Circular dichroism spectra (195 to 260 nm) were collected on a J-815 spectropolarimeter (JASCO Inc., Japan) to evaluate the secondary structure of the peptides and their complexes (*63*, *64*), individual peptides or complexes dissolved in PBS with the final concentration at 10 μM. Thermal denaturation of peptide complexes was monitored from 20° to 100°C at 222 nm with a thermal gradient of 5°C/min. The midpoint of the T_m values was acquired by JASCO software utilities.

Inhibition of pseudotyped virus infection

A pseudovirus bearing CoV S protein or VSV-G protein and a defective HIV-1 genome that expresses luciferase as reporter was produced in 293 T cells, as previously described (*27*), and its titer was quantitated by using HIV-1 p24 ELISA. The pseudovirus was then used to infect target Huh-7 cells (or ACE2/293 T cells for pseudotyped SARS-CoV) (10^4 per well in 96-well plates) in the presence or absence of the test peptide at the indicated concentration. Twelve hours after infection, culture medium was refreshed and then incubated for an additional 48 hours, followed by washing cells with PBS, lysing cells with lysis reagent (Promega), and transferring

Downloaded from http://advances.sciencemag.org/ on April 10, 2019

the cell lysates to 96-well Costar flat-bottom luminometer plates (Corning Costar) for the detection of relative light units using the Firefly Luciferase Assay Kit (Promega) and an Ultra 384 luminometer (Tecan).

Establishment of multiple HCoV S-mediated cell-cell fusion

As previously described (*27*), 293 T effector cells were transfected with plasmid pAAV-IRES-EGFP encoding the EGFP (293 T/EGFP cells) or plasmid pAAV-IRES-S-EGFP encoding the corresponding HCoV S protein (293 T/HCoV S/GFP cells) as the effector cells. Huh-7 cells, expressing various HCoV receptors on the membrane surface, were used as target cells, as described below.

1) *MERS-CoV S-mediated cell-cell fusion:* Effector cells (293 T/MERS-CoV/GFP) and target cells (Huh-7 cells) were cocultured in DMEM containing 10% FBS, at 37°C for 2 hours;

2) *229E S-mediated cell-cell fusion*: Effector cells (293 T/229E/GFP) and target cells (Huh-7 cells) were cocultured in DMEM containing 10% FBS, at 37°C for 4 hours;

3) *SARS-CoV and SL-CoV S-mediated cell-cell fusion*: Effector cells (293 T/SARS-CoV/GFP or 293 T/SL-CoV/GFP) and target cells (Huh-7 cells) were cocultured in the presence of trypsin (80 ng/ml) in DMEM without FBS, at 37°C for 4 hours;

4) *OC43 or NL63 S-mediated cell-cell fusion:* Effector cells (293 T/HCoV-OC43/GFP or 293 T/HCoV-NL63/GFP) and target cells (Huh-7 cells) were cocultured in the presence of trypsin (80 ng/ml) in DMEM without FBS, at 37°C for 4 hours.

Five fields in each well were randomly selected for counting the fused and unfused cells. The fused cells are at least twice as large as the unfused cells, and the fluorescence intensity in the fused cell became weak as a result of the diffusion of enhanced green fluorescent protein (EGFP) from one effector cell to target cells (see figs. S1D and S2C). The percentage of cell-cell fusion [(number of the fused cells/number of the fused and unfused cells) × 100%] was then calculated.

Inhibition of HCoV S-mediated cell-cell fusion

The inhibitory activity of a test peptide on HCoV S-mediated cell-cell fusion was determined, as previously described (*27*). Briefly, effector cells (293 T/S/GFP) and target cells (Huh-7 cells) were cocultured in the presence or absence of a test peptide at the indicated concentrations for fusion. After counting the fused and unfused cells, the percentage of cell-cell fusion was calculated, as described above. The percent inhibition of cell-cell fusion was calculated using the following formula as described elsewhere (*27*): $[1 - (E - N)/(P - N)] \times 100\%$. "*E*" represents the percentage of cell-cell fusion in the experimental group. "*P*" represents the percentage of cell-cell fusion in the positive control group, where 293 T/HCoV S/EGFP cells were used as effector cells, to which only PBS was added. "*N*" is the percentage of cell-cell fusion in negative control group, where 293 T/EGFP cells were used as effector cells. The IC_{50} was calculated using the CalcuSyn software provided by T. C. Chou (*65*). Samples were tested in triplicate, and all those experiments were repeated twice.

HCoV virion–based fusion assay

An HCoV virion–based fusion assay was performed, as described elsewhere (*34*, *35*). Briefly, Huh-7 cells and ACE2-293 T cells were used as target cells for the entry of MERS-CoV Blam-Vpr virions and SARS-CoV Blam-Vpr virions, respectively. These target cells were cultured at 37°C for 5 hours in six-well plates (with virions containing BlaM-Vpr equivalent to 80 ng of p24-Gag per well) in the presence or absence of EK1 at the indicated concentrations. The cells were washed with PBS, resuspended in 500 μl of DMEM, and then incubated with CCF4-AM substrate at room temperature for 2 hours, as described by the manufacturer (Invitrogen, Germany). Last, the cells were monitored via flow cytometry. After the virion fusion with the target cell, the CCF4-AM (emission at 520 nm) substrate could be cleaved by BlaM-Vpr into CCF4 (emission at 447 nm). Flow cytometric data were collected with a BD FACSDIVA and analyzed with FlowJo.

Inhibition of live HCoV's replication

The inhibitory activity of peptides against OC43 replication in HCT-8 cells was assessed, as described elsewhere (*66*). Briefly, 100 $TCID_{50}$ of OC43 was mixed with a test peptide at graded concentration and incubated at 37°C for 30 min. The mixture was then applied in triplicate onto the monolayer of HCT-8 cells grown in a 96-well microtiter plate. On day 5 after infection, viral titer in the culture medium was tested, and $TCID_{50}$ was calculated on the basis of the cytopathic effect (CPE) (*67*). The inhibitory activity of the tested peptide against 229E replication in A549 cells and NL63 replication in LLC-MK2 cells was evaluated in a similar way, as described above.

The inhibitory activity of peptide against MERS-CoV replication was tested in Calu-3 cells using a modified standard microneutralization assay, as previously described (*68*). Briefly, 60 μl of a serially twofold diluted peptide was incubated with 60 μl (120 $TCID_{50}$) of MERS-CoV in MEM medium supplemented with 2% FBS (M-2 medium) in duplicate wells of 96-well plates for ~60 min at room temperature. One hundred microliters of the peptide/MERS-CoV mixtures was then transferred into confluent Calu-3 cells grown in 96-well plates. Wells of Calu-3 cells cultured with M-2 medium with and without virus were included in these assays as positive and negative controls, respectively. While the advanced CPE of Calu-3 cells could develop within 24 to 36 hours in response to MERS-CoV infection at higher multiplicities of infection (MOIs) of 1 or 0.1 (*69*), we did not observe any prominent formation of CPE until ~ 60 to 72 hours after infection at an estimated MOI of ~ 0.001. Hence, to more accurately measure the efficacy of peptide inhibitors against MERS-CoV infection, we harvested the supernatants at 72 hours and quantified infectious virus titers by the standard Vero E6–based infectivity assays and expressed the titers as $\log_{10}$ $TCID_{50}$/ml.

Mouse infection studies

Pregnant Balb/c mice (18 days) purchased from the Department of Laboratory Animal Science, Fudan University were separated into four groups after delivery of their offspring. Eleven newborn mice were chosen for each group. Mice in the prevention and treatment groups were intranasally administered peptide (5 mg/kg in 2 μl of PBS) 30 min before or after intranasal challenge with a viral dose of 10^2 $TCID_{50}$ (in 2 μl DMEM). Mice in the viral control group and the normal control group were intranasally administered with 2 μl of PBS 30 min before viral challenge or without viral challenge. Mouse survival rate and body weight variations were recorded up to 2 weeks after infection (*70*). On day 5 after infection, five mice in each group were randomly selected for euthanasia to collect and assess the viral titer in mouse brain.

Briefly, mice expressing human DPP4 were randomly separated into three groups ($n = 6$): viral control, prophylactic group, and therapeutic

Downloaded from http://advances.sciencemag.org/ on April 10, 2019

group. In the viral control and therapeutic groups, each mouse was challenged intranasally with 10^4 $TCID_{50}$ [i.e., 1000 LD_{50} (median lethal dose)] of MERS-CoV in a volume of 60 μl, 30 min after viral challenge, and then treated via the intranasal route with 200 μg of EK1 (in 50 μl of PBS) or 50 μl of PBS, respectively. Prophylactic group mice were pretreated via the intranasal route with 200 μg of EK1 per mouse 30 min before viral challenge. Challenged mice were monitored daily for weight loss and mortality. In the interim, two mice were randomly euthanized (two of six) in each group at day 2 after challenge to determine the lung virus titers by CPE on Vero E6 and expressed as $TCID_{50}$/ml.

In vivo fluorescence imaging

Six Balb/c female mice (8 weeks old) were randomly assigned to two groups and nasally administered with 20 μg of Cy5-EK1 in 50 μl of PBS (n = 3) or 50 μl of PBS without peptide (n = 3) as control for background fluorescence measurement. One hour later, mice were imaged for distribution of Cy5-EK1 by the IVIS Lumina K Series III in vivo imaging system (PerkinElmer, Waltham, MA, USA). Mice were euthanized by intraperitoneal injection of sodium pentobarbital to obtain the lungs, livers, kidneys, spleens, and hearts for imaging and measuring their fluorescence value. The relevant radiant efficiency (P s^{-1} cm^{-2} sr^{-1}) (μW^{-1} cm^2) was then calculated by Living Image 4.4 software (*56*, *71*, *72*).

Cytotoxicity assay

Cytotoxicity of the peptides to the cells (293 T, 293 T/ACE2, Huh-7, A549, LLC-MK2, and Calu-3 cells) was tested by using the Cell Counting Kit-8 (CCK-8; Dojindo, Kumamoto, Japan). Briefly, each cell type was seeded into the wells of a 96-well microtiter plate (10^4 per well) and incubated at 37°C for 12 hours, replacing medium with DMED containing EK1 at graded concentrations. After incubation at 37°C for 2 days, CCK-8 solution (10 μl per well) was added, followed by an additional incubation for 4 hours. The absorbance was measured at 450 nm.

In vivo safety of EK1 through intranasal administration

As previously described (*27*), female Balb/c mice (8 weeks old) were assigned randomly to three groups (n = 5) and continuously administered with PBS, low-dose EK1 (20 mg/kg), or high-dose EK1 (100 mg/kg) by intranasal route every day for 1 week. The body weight changes were monitored for the following 2 weeks. ALT and creatinine in the sera of each group of mice were measured using the ALT and creatinine assay kits (NJJCBIO, Nanjing, China) before the first treatment and 1, 3, and 5 days after the final treatment. The titer of immunoglobulin G sera to EK1 in each group of mice was evaluated by ELISA 2 weeks after the final treatment. Four weeks after administration, mice in each group mice were euthanized to harvest the lungs, livers, kidneys, and spleens for hematoxylin and eosin staining. The animal studies were approved by the Institutional Laboratory Animal Care and Use Committee at Fudan University (20180302-019).

Statistical analyses

Analyses of independent data were performed by Student's unpaired two-tailed t test. Statistical analyses were carried out using GraphPad Prism 6.0. P values less than 0.05 were considered significant; $^*P < 0.05$, $^{**}P < 0.01$, $^{***}P < 0.001$, and $^{****}P < 0.0001$. The IC_{50} was calculated using the CalcuSyn software (*65*).

SUPPLEMENTARY MATERIALS

Supplementary material for this article is available at http://advances.sciencemag.org/cgi/content/full/5/4/eaav4580/DC1

Fig. S1. Interaction between HCoV HR1 and HR2 regions in HCoV S proteins.
Fig. S2. Identity and similarity in spike protein sequences of SARS-CoV and SL-CoVs and the effect of EK1 on HCoV S protein–mediated cell fusion and virus-cell fusion, as well as the viral loads and histopathological changes in brains of HCoV-infected mice.
Fig. S3. In vivo safety of EK1 through intranasal administration.
Fig. S4. Structural comparison between the HR1-EK1 6-HB bundles and cognate HR1-HR2 6-HB bundles reveals that the EK1 peptide binds to the triple-helix HR1 core of different HCoVs in a similar manner to that of the native HR2 of the corresponding HCoV.
Fig. S5. The EK1 peptide forms 6-helical bundle structures with the HR1 motifs from OC43, HKU1, and NL63.
Fig. S6. Interactions between the HR1 and HR2 motifs of MERS and 229E.
Fig. S7. Key residues at critical positions endow EK1 and OC43-HR2 with pan-CoV activity.
Table S1. Inhibitory activity of peptides on multiple cell-cell fusion assays.
Table S2. Solubility and fusion inhibitory activities of different peptides.
Table S3. Data collection and structural refinement statistics.

REFERENCES AND NOTES

1. P. C. Y. Woo, S. K. P. Lau, C. S. F. Lam, C. C. Y. Lau, A. K. L. Tsang, J. H. N. Lau, R. Bai, J. L. L. Teng, C. C. C. Tsang, M. Wang, B.-J. Zheng, K.-H. Chan, K.-Y. Yuen, Discovery of seven novel mammalian and avian coronaviruses in the genus *Deltacoronavirus* supports bat coronaviruses as the gene source of *Alphacoronavirus* and *Betacoronavirus* and avian coronaviruses as the gene source of *Gammacoronavirus* and *Deltacoronavirus*. *J. Virol.* **86**, 3995–4008 (2012).
2. S. Su, G. Wong, W. Shi, J. Liu, A. C. K. Lai, J. Zhou, W. Liu, Y. H. Bi, G. F. Gao, Epidemiology, genetic recombination, and pathogenesis of coronaviruses. *Trends Microbiol.* **24**, 490–502 (2016).
3. A. Simon, S. Völz, K. Höfling, A. Kehl, R. Tillman, A. Müller, B. Kupfer, A.-M. Eis-Hübinger, M. J. Lentze, U. Bode, O. Schildgen, Acute life threatening event (ALTE) in an infant with human coronavirus HCoV-229E infection. *Pediatr. Pulmonol.* **42**, 393–396 (2007).
4. S. Morfopoulou, J. R. Brown, E. G. Davies, G. Anderson, A. Virasami, W. Qasim, W. K. Chong, M. Hubank, V. Plagnol, M. Desforges, T. S. Jacques, P. J. Talbot, J. Breuer, Human coronavirus OC43 associated with fatal encephalitis. *N. Engl. J. Med.* **375**, 497–498 (2016).
5. K. Mayer, C. Nellessen, C. Hahn-Ast, M. Schumacher, S. Pietzonka, A. M. Eis-Hübinger, C. Drosten, P. Brossart, D. Wolf, Fatal outcome of human coronavirus NL63 infection despite successful viral elimination by IFN-alpha in a patient with newly diagnosed ALL. *Eur. J. Haematol.* **97**, 208–210 (2016).
6. M. N. Al-Khannaq, K. T. Ng, X. Y. Oong, Y. K. Pang, Y. Takebe, J. B. Chook, N. S. Hanafi, A. Kamarulzaman, K. K. Tee, Molecular epidemiology and evolutionary histories of human coronavirus OC43 and HKU1 among patients with upper respiratory tract infections in Kuala Lumpur, Malaysia. *Virol. J.* **13**, 33 (2016).
7. X. Y. Oong, K. T. Ng, Y. Takebe, L. J. Ng, K. G. Chan, J. B. Chook, A. Kamarulzaman, K. K. Tee, Identification and evolutionary dynamics of two novel human coronavirus OC43 genotypes associated with acute respiratory infections: Phylogenetic, spatiotemporal and transmission network analyses. *Emerg. Microbes Infect.* **6**, e3 (2017).
8. S. K. P. Lau, P. Lee, A. K. L. Tsang, C. C. Y. Yip, H. Tse, R. A. Lee, L.-Y. So, Y.-L. Lau, K.-H. Chan, P. C. Y. Woo, K.-Y. Yuen, Molecular epidemiology of human coronavirus OC43 reveals evolution of different genotypes over time and recent emergence of a novel genotype due to natural recombination. *J. Virol.* **85**, 11325–11337 (2011).
9. V. D. Menachery, B. L. Yount Jr., K. Debbink, S. Agnihothram, L. E. Gralinski, J. A. Plante, R. L. Graham, T. Scobey, X.-Y. Ge, E. F. Donaldson, S. H. Randell, A. Lanzavecchia, W. A. Marasco, Z.-L. Shi, R. S. Baric, A SARS-like cluster of circulating bat coronaviruses shows potential for human emergence. *Nat. Med.* **21**, 1508–1513 (2015).
10. X.-Y. Ge, J.-L. Li, X.-L. Yang, A. A. Chmura, G. Zhu, J. H. Epstein, J. K. Mazet, B. Hu, W. Zhang, C. Peng, Y.-J. Zhang, C.-M. Luo, B. Tan, N. Wang, Y. Zhu, G. Crameri, S.-Y. Zhang, L.-F. Wang, P. Daszak, Z.-L. Shi, Isolation and characterization of a bat SARS-like coronavirus that uses the ACE2 receptor. *Nature* **503**, 535–538 (2013).
11. V. D. Menachery, B. L. Yount Jr., A. C. Sims, K. Debbink, S. S. Agnihothram, L. E. Gralinski, R. L. Graham, T. Scobey, J. A. Plante, S. R. Royal, J. Swanstrom, T. P. Sheahan, R. J. Pickles, D. Corti, S. H. Randell, A. Lanzavecchia, W. A. Marasco, R. S. Baric, SARS-like WIV1-CoV poised for human emergence. *Proc. Natl. Acad. Sci. U.S.A.* **113**, 3048–3053 (2016).
12. Y. Yang, C. Liu, L. Y. Du, S. Jiang, Z. Shi, R. S. Baric, F. Li, Two mutations were critical for bat-to-human transmission of Middle East Respiratory Syndrome coronavirus. *J. Virol.* **89**, 9119–9123 (2015).
13. P. C. Y. Woo, S. K. P. Lau, K. S. M. Li, A. K. L. Tsang, K.-Y. Yuen, Genetic relatedness of the novel human group C betacoronavirus to *Tylonycteris* bat coronavirus HKU4 and *Pipistrellus* bat coronavirus HKU5. *Emerg. Microbes Infect.* **1**, e35 (2012).

Downloaded from http://advances.sciencemag.org/ on April 10, 2019

14. G. Lu, Q. Wang, G. F. Gao, Bat-to-human: Spike features determining 'host jump' of coronaviruses SARS-CoV, MERS-CoV, and beyond. *Trends Microbiol.* **23**, 468–478 (2015).
15. S. Xia, Q. Liu, Q. Wang, Z. Sun, S. Su, L. Du, T. Ying, L. Lu, S. Jiang, Middle East respiratory syndrome coronavirus (MERS-CoV) entry inhibitors targeting spike protein. *Virus Res.* **194**, 200–210 (2014).
16. S. Jiang, L. Lu, Q. Liu, W. Xu, L. Du, Receptor-binding domains of spike proteins of emerging or re-emerging viruses as targets for development of antiviral vaccines. *Emerg. Microbes Infect.* **1**, e13 (2012).
17. J. Sui, M. Deming, B. Rockx, R. C. Liddington, Q. K. Zhu, R. S. Baric, W. A. Marasco, Effects of human anti-spike protein receptor binding domain antibodies on severe acute respiratory syndrome coronavirus neutralization escape and fitness. *J. Virol.* **88**, 13769–13780 (2014).
18. S. Liu, G. Xiao, Y. Chen, Y. He, J. K. Niu, C. R. Escalante, H. Xiong, J. Farmar, A. K. Debnath, P. Tien, S. Jiang, Interaction between heptad repeat 1 and 2 regions in spike protein of SARS-associated coronavirus: Implications for virus fusogenic mechanism and identification of fusion inhibitors. *Lancet* **363**, 938–947 (2004).
19. S. Jiang, K. Lin, N. Strick, A. R. Neurath, HIV-1 inhibition by a peptide. *Nature* **365**, 113 (1993).
20. C. T. Wild, D. C. Shugars, T. K. Greenwell, C. B. Mcdanal, T. J. Matthews, Peptides corresponding to a predictive alpha-helical domain of human-immunodeficiency-virus type 1 gp41 are potent inhibitors of virus-infection. *Proc. Natl. Acad. Sci. U.S.A.* **91**, 9770–9774 (1994).
21. M. Lu, P. S. Kim, A trimeric structural subdomain of the HIV-1 transmembrane glycoprotein. *J. Biomol. Struct. Dynam.* **15**, 465–471 (1997).
22. M. K. Lawless-Delmedico, P. Sista, R. Sen, N. C. Moore, J. B. Antczak, J. M. White, R. J. Greene, K. C. Leanza, T. J. Matthews, D. M. Lambert, Heptad-repeat regions of respiratory syncytial virus F_1 protein form a six-membered coiled-coil complex. *Biochemistry* **39**, 11684–11695 (2000).
23. S. Watanabe, A. Takada, T. Watanabe, H. Ito, H. Kida, Y. Kawaoka, Functional importance of the coiled-coil of the Ebola virus glycoprotein. *J. Virol.* **74**, 10194–10201 (2000).
24. C. J. Russell, T. S. Jardetzky, R. A. Lamb, Membrane fusion machines of paramyxoviruses: Capture of intermediates of fusion. *EMBO J.* **20**, 4024–4034 (2001).
25. K. N. Bossart, B. A. Mungall, G. Crameri, L.-F. Wang, B. T. Eaton, C. C. Broder, Inhibition of *Henipavirus* fusion and infection by heptad-derived peptides of the *Nipah* virus fusion glycoprotein. *Virol. J.* **2**, 57 (2005).
26. B. J. Bosch, R. van der Zee, C. A. M. de Haan, P. J. M. Rottier, The coronavirus spike protein is a class I virus fusion protein: Structural and functional characterization of the fusion core complex. *J. Virol.* **77**, 8801–8811 (2003).
27. L. Lu, Q. Liu, Y. Zhu, K.-H. Chan, L. Qin, Y. Li, Q. Wang, J. F.-W. Chan, L. Du, F. Yu, C. Ma, S. Ye, K.-Y. Yuen, R. Zhang, S. Jiang, Structure-based discovery of Middle East respiratory syndrome coronavirus fusion inhibitor. *Nat. Commun.* **5**, 3067 (2014).
28. H. Aydin, D. Al-Khooly, J. E. Lee, Influence of hydrophobic and electrostatic residues on SARS-coronavirus S2 protein stability: Insights into mechanisms of general viral fusion and inhibitor design. *Protein Sci.* **23**, 603–617 (2014).
29. Q. Zheng, Y. Deng, J. Liu, L. van der Hoek, B. Berkhout, M. Lu, Core structure of S2 from the human coronavirus NL63 spike glycoprotein. *Biochemistry* **45**, 15205–15215 (2006).
30. A. Otaka, M. Nakamura, D. Nameki, E. Kodama, S. Uchiyama, S. Nakamura, H. Nakano, H. Tamamura, Y. Kobayashi, M. Matsuoka, N. Fujii, Remodeling of gp41-C34 peptide leads to highly effective inhibitors of the fusion of HIV-1 with target cells. *Angew. Chem. Int. Ed.* **41**, 2937–2940 (2002).
31. S. Marqusee, R. L. Baldwin, Helix stabilization by Glu-…Lys+ salt bridges in short peptides of de novo design. *Proc. Natl. Acad. Sci. U.S.A.* **84**, 8898–8902 (1987).
32. F. Li, W. Li, M. Farzan, S. C. Harrison, Structure of SARS coronavirus spike receptor-binding domain complexed with receptor. *Science* **309**, 1864–1868 (2005).
33. R. Channappanavar, L. Lu, S. Xia, L. Du, D. K. Meyerholz, S. Perlman, S. Jiang, Protective effect of intranasal regimens containing peptidic Middle East respiratory syndrome coronavirus fusion inhibitor against MERS-CoV infection. *J. Infect. Dis.* **212**, 1894–1903 (2015).
34. M. Cavrois, C. de Noronha, W. C. Greene, A sensitive and specific enzyme-based assay detecting HIV-1 virion fusion in primary T lymphocytes. *Nat. Biotechnol.* **20**, 1151–1154 (2002).
35. M. Cavrois, J. Neidleman, W. Yonemoto, D. Fenard, W. C. Greene, HIV-1 virion fusion assay: Uncoating not required and no effect of Nef on fusion. *Virology* **328**, 36–44 (2004).
36. A. Yonezawa, M. Cavrois, W. C. Greene, Studies of Ebola virus glycoprotein-mediated entry and fusion by using pseudotyped human immunodeficiency virus type 1 virions: Involvement of cytoskeletal proteins and enhancement by tumor necrosis factor alpha. *J. Virol.* **79**, 918–926 (2005).
37. M. C. Wolf, Y. Wang, A. N. Freiberg, H. C. Aguilar, M. R. Holbrook, B. Lee, A catalytically and genetically optimized β-lactamase-matrix based assay for sensitive, specific, and higher throughput analysis of native henipavirus entry characteristics. *Virol. J.* **6**, 119 (2009).
38. L. Yan, B. Meng, J. Xiang, I. A. Wilson, B. Yang, Crystal structure of the post-fusion core of the human coronavirus 229E spike protein at 1.86 Å resolution. *Acta Crystallogr. D* **74**, 841–851 (2018).
39. T. Ying, L. Du, T. W. Ju, P. Prabakaran, C. C. Y. Lau, L. Lu, Q. Liu, L. Wang, Y. Feng, Y. Wang, B.-J. Zheng, K.-Y. Yuen, S. Jiang, D. S. Dimitrov, Exceptionally potent neutralization of Middle East respiratory syndrome coronavirus by human monoclonal antibodies. *J. Virol.* **88**, 7796–7805 (2014).
40. W. Tai, Y. Wang, C. A. Fett, G. Zhao, F. Li, S. Perlman, S. Jiang, Y. Zhou, L. Du, Recombinant receptor-binding domains of multiple Middle East respiratory syndrome coronaviruses (MERS-CoVs) induce cross-neutralizing antibodies against divergent human and camel MERS-CoVs and antibody escape mutants. *J. Virol.* **91**, e01651-16 (2017).
41. L. Wang, W. Shi, J. D. Chappell, M. G. Joyce, Y. Zhang, M. Kanekiyo, M. M. Becker, N. van Doremalen, R. Fischer, N. Wang, K. S. Corbett, M. Choe, R. D. Mason, J. G. Van Galen, T. Zhou, K. O. Saunders, K. M. Tatti, L. M. Haynes, P. D. Kwong, K. Modjarrad, W.-P. Kong, J. S. McLellan, M. R. Denison, V. J. Munster, J. R. Mascola, B. S. Graham, Importance of neutralizing monoclonal antibodies targeting multiple antigenic sites on MERS-CoV spike glycoprotein to avoid neutralization escape. *J. Virol.* **92**, e02002-17 (2018).
42. F. Li, Receptor recognition mechanisms of coronaviruses: A decade of structural studies. *J. Virol.* **89**, 1954–1964 (2015).
43. B. J. Bosch, B. E. E. Martina, R. van der Zee, J. Lepault, B. J. Haijema, C. Versluis, A. J. R. Heck, R. de Groot, A. D. M. E. Osterhaus, P. J. M. Rottier, Severe acute respiratory syndrome coronavirus (SARS-CoV) infection inhibition using spike protein heptad repeat-derived peptides. *Proc. Natl. Acad. Sci. U.S.A.* **101**, 8455–8460 (2004).
44. S. Liu, W. Jing, B. Cheung, H. Lu, J. Sun, X. Yan, J. Niu, J. Farmar, S. Wu, S. Jiang, HIV gp41 C-terminal heptad repeat contains multifunctional domains. Relation to mechanisms of action of anti-HIV peptides. *J. Biol. Chem.* **282**, 9612–9620 (2007).
45. C. Wang, L. Zhao, S. Xia, T. Zhang, R.-Y. Cao, G. Liang, Y. Li, G. Meng, W. Wang, W. Shi, W. Zhong, S. Jiang, K. Liu, De novo design of α-helical lipopeptides targeting viral fusion proteins: A promising strategy for relatively broad-spectrum antiviral drug discovery. *J. Med. Chem.* **61**, 8734–8745 (2018).
46. C. Wang, S. Xia, P. Zhang, T. Zhang, W. Wang, Y. Tian, G. Meng, S. Jiang, K. Liu, Discovery of hydrocarbon-stapled short α-helical peptides as promising middle east respiratory syndrome coronavirus (MERS-CoV) fusion inhibitors. *J. Med. Chem.* **61**, 2018–2026 (2018).
47. S. Matsuyama, N. Nagata, K. Shirato, M. Kawase, M. Takeda, F. Taguchi, Efficient activation of the severe acute respiratory syndrome coronavirus spike protein by the transmembrane protease TMPRSS2. *J. Virol.* **84**, 12658–12664 (2010).
48. J. T. Earnest, M. P. Hantak, K. Li, P. B. McCray Jr., S. Perlman, T. Gallagher, The tetraspanin CD9 facilitates MERS-coronavirus entry by scaffolding host cell receptors and proteases. *PLOS Pathog.* **13**, e1006546 (2017).
49. S. Bertram, I. Glowacka, M. A. Müller, H. Lavender, K. Gnirss, I. Nehlmeier, D. Niemeyer, Y. He, G. Simmons, C. Drosten, E. J. Soilleux, O. Jahn, I. Steffen, S. Pöhlmann, Cleavage and activation of the severe acute respiratory syndrome coronavirus spike protein by human airway trypsin-like protease. *J. Virol.* **85**, 13363–13372 (2011).
50. S.-Y. Choi, S. Bertram, I. Glowacka, Y. W. Park, S. Pöhlmann, Type II transmembrane serine proteases in cancer and viral infections. *Trends Mol. Med.* **15**, 303–312 (2009).
51. K. Shirato, K. Kanou, M. Kawase, S. Matsuyama, Clinical isolates of human coronavirus 229E bypass the endosome for cell entry. *J. Virol.* **91**, e01387-16 (2017).
52. K. Shirato, M. Kawase, S. Matsuyama, Wild-type human coronaviruses prefer cell-surface TMPRSS2 to endosomal cathepsins for cell entry. *Virology* **517**, 9–15 (2018).
53. S. S. Chiu, K. H. Chan, K. W. Chu, S. W. Kwan, Y. Guan, L. L. M. Poon, J. S. M. Peiris, Human coronavirus NL63 infection and other coronavirus infections in children hospitalized with acute respiratory disease in Hong Kong, China. *Clin. Infect. Dis.* **40**, 1721–1729 (2005).
54. G. J. Gorse, T. Z. O'Connor, S. L. Hall, J. N. Vitale, K. L. Nichol, Human coronavirus and acute respiratory illness in older adults with chronic obstructive pulmonary disease. *J. Infect. Dis.* **199**, 847–857 (2009).
55. A. Jean, C. Quach, A. Yung, M. Semret, Severity and outcome associated with human coronavirus OC43 infections among children. *Pediatr. Infect. Dis. J.* **32**, 325–329 (2013).
56. Y. Yu, Y.-Q. Deng, P. Zou, Q. Wang, Y. Dai, F. Yu, L. Du, N.-N. Zhang, M. Tian, J.-N. Hao, Y. Meng, Y. Li, X. Zhou, J. F.-W. Chan, K.-Y. Yuen, C.-F. Qin, S. Jiang, L. Lu, A peptide-based viral inactivator inhibits Zika virus infection in pregnant mice and fetuses. *Nat. Commun.* **8**, 15672 (2017).
57. Z. Otwinowski, W. Minor, Processing of X-ray diffraction data collected in oscillation mode. *Methods Enzymol.* **276**, 307–326 (1997).
58. P. D. Adams, P. V. Afonine, G. Bunkóczi, V. B. Chen, I. W. Davis, N. Echols, J. J. Headd, L.-W. Hung, G. J. Kapral, R. W. Grosse-Kunstleve, A. J. McCoy, N. W. Moriarty, R. Oeffner, R. J. Read, D. C. Richardson, J. S. Richardson, T. C. Terwilliger, P. H. Zwart, PHENIX: A comprehensive Python-based system for macromolecular structure solution. *Acta Crystallogr. D* **66**, 213–221 (2010).
59. P. Emsley, K. Cowtan, Coot: Model-building tools for molecular graphics. *Acta Crystallogr. D* **60**, 2126–2132 (2004).

Downloaded from http://advances.sciencemag.org/ on April 10, 2019

60. V. B. Chen, W. B. Arendall III, J. J. Headd, D. A. Keedy, R. M. Immormino, G. J. Kapral, L. W. Murray, J. S. Richardson, D. C. Richardson, MolProbity: All-atom structure validation for macromolecular crystallography. *Acta Crystallogr. D* **66**, 12–21 (2010).
61. T. J. Dolinsky, J. E. Nielsen, J. A. McCammon, N. A. Baker, PDB2PQR: An automated pipeline for the setup of Poisson-Boltzmann electrostatics calculations. *Nucleic Acids Res.* **32**, W665–W667 (2004).
62. M. Biasini, S. Bienert, A. Waterhouse, K. Arnold, G. Studer, T. Schmidt, F. Kiefer, T. G. Cassarino, M. Bertoni, L. Bordoli, T. Schwede, SWISS-MODEL: Modelling protein tertiary and quaternary structure using evolutionary information. *Nucleic Acids Res.* **42**, W252–W258 (2014).
63. Y. H. Chen, J. T. Yang, K. H. Chau, Determination of the helix and beta form of proteins in aqueous solution by circular dichroism. *Biochemistry* **13**, 3350–3359 (1974).
64. S. W. Liu, Q. Zhao, S. B. Jiang, Determination of the HIV-1 gp41 fusogenic core conformation modeled by synthetic peptides: Applicable for identification of HIV-1 fusion inhibitors. *Peptides* **24**, 1303–1313 (2003).
65. T.-C. Chou, Theoretical basis, experimental design, and computerized simulation of synergism and antagonism in drug combination studies. *Pharmacol. Rev.* **58**, 621–681 (2006).
66. E. Brison, H. Jacomy, M. Desforges, P. J. Talbot, Novel treatment with neuroprotective and antiviral properties against a neuroinvasive human respiratory virus. *J. Virol.* **88**, 1548–1563 (2014).
67. J. Ciejka, K. Wolski, M. Nowakowska, K. Pyrc, K. Szczubiałka, Biopolymeric nano/microspheres for selective and reversible adsorption of coronaviruses. *Mater. Sci. Eng. C Mater. Biol. Appl.* **76**, 735–742 (2017).
68. X. Tao, F. Mei, A. Agrawal, C. J. Peters, T. G. Ksiazek, X. Cheng, C.-T. K. Tseng, Blocking of exchange proteins directly activated by cAMP leads to reduced replication of Middle East respiratory syndrome coronavirus. *J. Virol.* **88**, 3902–3910 (2014).
69. X. Tao, T. E. Hill, C. Morimoto, C. J. Peters, T. G. Ksiazek, C.-T. K. Tseng, Bilateral entry and release of Middle East respiratory syndrome coronavirus induces profound apoptosis of human bronchial epithelial cells. *J. Virol.* **87**, 9953–9958 (2013).
70. H. Jacomy, P. J. Talbot, Vacuolating encephalitis in mice infected by human coronavirus OC43. *Virology* **315**, 20–33 (2003).
71. S. Tomcin, G. Baier, K. Landfester, V. Mailänder, Pharmacokinetics on a microscale: Visualizing Cy5-labeled oligonucleotide release from poly(*n*- butylcyanoacrylate) nanocapsules in cells. *Int. J. Nanomedicine* **9**, 5471–5489 (2014).
72. M. Q. Tan, S. M. Burden-Gulley, W. Li, X. M. Wu, D. Lindner, S. M. Brady-Kalnay, V. Gulani, Z.-R. Lu, MR molecular imaging of prostate cancer with a peptide-targeted contrast agent in a mouse orthotopic prostate cancer model. *Pharm. Res.* **29**, 953–960 (2012).

Acknowledgments: We thank F. Li at the University of Minnesota Medical School for providing the HCoV-229E and HCoV-NL63 spike gene. We thank the staff from BL19U1 beamline of the National Facility for Protein Science Shanghai (NFPS) at the Shanghai Synchrotron Radiation Facility for assistance during data collection. **Funding:** This work was supported by the National Megaprojects of China for Major Infectious Diseases (2018ZX10301403 to L.L.), the Ministry of Science and Technology of the People's Republic of China (2016YFC1201000 and 2016YFC1200405 to S.J. and 2016YFC1202901 to L.L.), the National Natural Science Foundation of China (81661128041, 81672019, and 81822045 to L.L. and 31600619 to B.Y.), the Shanghai Rising-Star Program (16QA1400300 to L.L.), and the Sanming Project of Medicine in Shenzhen (to S.J.). **Author contributions:** L.L., B.Y., S.J., and I.A.W. designed the study. S.X. established the cell-cell fusion assays, performed the inhibition of HCoV-OC43 infection in vivo and in vitro assays and EK1 safety study, and conducted circular dichroism spectroscopy and cytotoxicity assay. B.Y. and L.Y. performed the expression and purification of fusion protein HR1-L6-EK1 and structural study. S.X., W.X., Q.W., and L.D. prepared cells and viruses and conducted the pseudotyped and live virus infection assays. A.S.A. and A.S. performed the inhibition of MERS-CoV infection in vivo and in vitro assays. L.L., B.Y., W.X., S.J., W.T., I.A.W., and C.-T.K.T. analyzed the data. S.X., L.L., B.Y., S.J., W.T., I.A.W., and C.-T.K.T. wrote the paper. **Competing interests**: S.J., L.L., S.X., Q.W., and W.X. are inventors on a patent application related to this work assigned to Fudan University (application no. CN201610070216.4, filed on 30 January 2016, published on 8 August 2017, publication no. CN107022008A). The other authors declare that they have no competing interests. **Data and materials availability:** All data needed to evaluate the conclusions in the paper are present in the paper and/or the Supplementary Materials. Additional data related to this paper may be requested from the authors. Coordinates and structure factors of the crystal structures of the EK1 complexes with HR1 from SARS, MERS, and 229E have been deposited in the PDB with IDs 5zvm, 5zvk, and 5zuv, respectively.

Submitted 25 September 2018
Accepted 14 February 2019
Published 10 April 2019
10.1126/sciadv.aav4580

Citation: S. Xia, L. Yan, W. Xu, A. S. Agrawal, A. Algaissi, C.-T. K. Tseng, Q. Wang, L. Du, W. Tan, I. A. Wilson, S. Jiang, B. Yang, L. Lu, A pan-coronavirus fusion inhibitor targeting the HR1 domain of human coronavirus spike. *Sci. Adv.* **5**, eaav4580 (2019).

Downloaded from http://advances.sciencemag.org/ on April 10, 2019

Science Advances

A pan-coronavirus fusion inhibitor targeting the HR1 domain of human coronavirus spike

Shuai Xia, Lei Yan, Wei Xu, Anurodh Shankar Agrawal, Abdullah Algaissi, Chien-Te K. Tseng, Qian Wang, Lanying Du, Wenjie Tan, Ian A. Wilson, Shibo Jiang, Bei Yang and Lu Lu

Sci Adv **5** (4), eaav4580.
DOI: 10.1126/sciadv.aav4580

ARTICLE TOOLS http://advances.sciencemag.org/content/5/4/eaav4580

SUPPLEMENTARY MATERIALS http://advances.sciencemag.org/content/suppl/2019/04/08/5.4.eaav4580.DC1

REFERENCES This article cites 72 articles, 25 of which you can access for free
http://advances.sciencemag.org/content/5/4/eaav4580#BIBL

PERMISSIONS http://www.sciencemag.org/help/reprints-and-permissions

Use of this article is subject to the Terms of Service

Science Advances (ISSN 2375-2548) is published by the American Association for the Advancement of Science, 1200 New York Avenue NW, Washington, DC 20005. 2017 © The Authors, some rights reserved; exclusive licensee American Association for the Advancement of Science. No claim to original U.S. Government Works. The title *Science Advances* is a registered trademark of AAAS.

Downloaded from http://advances.sciencemag.org/ on April 10, 2019